2021

SEISMOTECTONIC INTERPRETATION OF AN EXPANSIVE SET OF EARTHQUAKE FOCAL MECHANISMS FROM FIRST MOTIONS AND AMPLITUDE RATIOS ON THE YELLOWSTONE PLATEAU

Cristhian Salas Pazmiño
Michigan Technological University, csalas@mtu.edu

SEISMOTECTONIC INTERPRETATION OF AN EXPANSIVE SET OF EARTHQUAKE FOCAL MECHANISMS FROM FIRST MOTIONS AND AMPLITUDE RATIOS ON THE YELLOWSTONE PLATEAU

By

Cristhian Paul Salas Pazmiño

A THESIS

Submitted in partial fulfillment of the requirements for the degree of

MASTER OF SCIENCE

In Geophysics

MICHIGAN TECHNOLOGICAL UNIVERSITY

2021

This thesis has been approved in partial fulfillment of the requirements for the Degree of MASTER OF SCIENCE in Geophysics.

Department of Geological and Mining Engineering and Sciences

Thesis Advisor: *Gregory P. Waite*

Committee Member: *Aleksey Smirnov*

Committee Member: *Radwin Askari*

Department Chair: *Aleksey Smirnov*

Table of Contents

List of Figures

List of tables

Acknowledgments

I would first like to thank my thesis advisor Greg Waite for his unconditional support and patience. He consistently allowed this thesis to be my own work but steered me in the right direction whenever he thought I needed it.

I would like to especially thank Ms. Lina Taskovich and her family for funding the Natale & Maria Louisa Tormen Endowed Scholarship that funded my master's program at Michigan Tech. Any of this would not have possible without their support.

Finally, I must express my very profound gratitude to my family and friends especially to Katie and Nel for providing me with unfailing support and continuous encouragement during these last almost 2 years and through the process of researching and writing this thesis. This accomplishment would not have been possible without them. Thank you very much!

Abstract

We present high-quality focal mechanisms and stress inversions based on a refined earthquake location catalog for the Yellowstone Plateau. The relocation process is based on non-linear search techniques that use three-dimensional velocity models. The original catalog contained 18,940 events between January 2010 and March 2021 and was obtained from the University of Utah Seismograph Stations. We successfully relocate 7735 earthquakes and use this information to calculate the focal mechanisms by using two approaches. First, we only consider the P-wave first motion polarities and use the HASH program. For the second approach, we include the S-wave/P-wave amplitude ratios and evaluate if they can improve the computed focal mechanisms obtained using only P-wave first motion polarities. We filter the results to create a subset of data with the best quality solutions. Finally, we run joint inversion for stress and fault orientations from focal mechanisms using the STRESSINVERSE package. We divide the study area into smaller sections to analyze the spatial and temporal variations of the seismic stress field. Overall, the inclusion of the amplitude ratios proved to be efficient at improving the low-quality events, but it is inefficient at refining solutions with previously established good quality solutions. The stress field in this area presents temporal variations that are associated with the uplift and subsidence processes. The Yellowstone Plateau also displays spatial variations. To describe these variations, we use the minimum principal stress directions that are horizontal or near horizontal in all the cases as expected for an extensional regime dominated by NE-SW Basin and Range extension in this area. The minimum stress direction rotates from an orientation near to N-S near Hebgen Lake fault zone to NE-SW near Norris Junction. In addition, all the regions that fall within the 0.64 Ma caldera display orientations ENE-WSW.

1 Introduction

Earthquake locations and the computation of focal mechanisms are the most widely used seismic parameters to reveal stress directions in tectonically and volcanically active regions like the Yellowstone Plateau [Lin and Okubo, 2016]. Crucial information about deep fault structure and the stress field of an area can be inferred from the fault-plane orientations and slip directions of earthquakes [e.g., Hardebeck and Shearer, 2002; Hardebeck and Shearer, 2003; Lin and Okubo, 2016]. Earthquake focal mechanism inversion is one of the methods available for determining principal stress directions at seismogenic depths [Maury et al., 2013]. In this study, we calculated the focal mechanisms from a relocated earthquake catalog and subsequently invert these results for stress to identify spatial and temporal variations between January 2010 and March 2021. This section will introduce the geologic setting of the study area and some other general concepts.

1.1 Geological setting

The Yellowstone volcanic field is the youngest manifestation of the interaction of the North American Plate moving southwestward across a mantle plume that created the 16-17 Ma, 700-km-long Yellowstone-Snake River Plain (YSRP) a silicic volcanic system [Huang et al., 2015; Smith et al., 2009]. It is located at the eastern edge of the tectonically active 30 Ma Basin and Range Province, an 800-km-wide intraplate region of the western US. This region is characterized by dominant normal to oblique-slip faulting and lithospheric extension [Smith et al., 2009; Russo et al., 2017]. This volcanic system is one of the largest silicic volcanic systems globally and has experienced three large, caldera-forming eruptions at the Yellowstone Plateau in the last 2 Ma. The caldera-forming eruptions occurred at 2.0, 1.3, and the most recent eruption occurred 0.64 Ma and formed the 45km by 70 km long Yellowstone caldera [Christiansen, 2001; Farrell et al., 2014; Waite and Smith, 2004]. In addition, two resurgent domes were formed by a post-collapse

uplift: the eastern Sour Creek dome became resurgent soon after collapse, and the western 0.16 Ma Mallard Lake dome [Christiansen, 2001; Russo et al., 2017].

The Yellowstone Plateau has been the source of some of the largest Quaternary eruptions on Earth. More than 140 giant silicic eruptions associated with the YSRP have been identified by the tephrachronology of ash-fall tuffs [Perkinsand Nash, 2002; Smith et al., 2009]. The last episode of explosive volcanism was followed by ~60 smaller bimodal basalt-rhyolite eruptions, with the most recent occurring 70,000 years ago. Moreover, Yellowstone exhibits the largest concentration of hydrothermal features in the world. It is also characterized by many seismic events and extraordinarily high heat flow ~ 2000 m Wm−2. Finally, this area has experienced episodes of uplift and subsidence with rates of up to 7 cm/yr. [Christiansen, 2001; Farrel et al., 2014].

1.2 Previous studies

Several studies have been carried out to determine the stress field of the Yellowstone Plateau area by using seismic data, including focal mechanisms and stress inversions. In 2004, Waite and Smith analyzed the spatial variation of the stress field at Yellowstone by examining source mechanisms of 25 years of network-recorded earthquakes between 1973–1998. The authors determined a rotation of the tension (T) axes from NNE-SSW near Hebgen Lake to ENE-WSW 35 km east of there. They also performed stress inversions using first-motion polarities and revealed a similar pattern in the minimum principal stress orientations [Waite and Smith, 2004].

In 2009, White et al. used first motion P-wave focal mechanisms to determine the stress model for the Teton region, located south of the Yellowstone Plateau. The authors also analyzed the spatial variation of their study area to find possible variations of the stress field. As a result, they revealed a dominant E–W extension across the Teton fault with a NE–SW extension along southern Yellowstone and the northern Teton fault area [White et al., 2009].

In 2017, Russo et al. used a set of 369 well-constrained, double-couple, focal mechanism solutions obtained from earthquake relocations to evaluate the spatial and temporal variation of the stress field. The catalog contained data between 1988 through the beginning of 2010. The authors obtained stress-field inversions by using the earthquake focal mechanisms. They revealed a well-resolved rotation of σ3 from NNE-SSW near the Hebgen Lake fault zone to ENE-WSW near Norris Junction. They also found that the σ3 direction changed over the years at the Norris Geyser Basin, from ENE-WSW, as calculated by Waite and Smith (2004), to NNE-SSW. Finally, they also found that the other σ3 directions did not change over time.

In 2019, Shelly and Hardebeck examined the 2017 Yellowstone Maple Creek Earthquake Swarm. To gain insight into the swarm, they enhanced the routine seismic catalog to include many smaller earthquakes and relocate all the events. In total, they located nearly 16,000 earthquakes and estimated magnitudes for more than 30,000 events. Furthermore, they used correlation measurements to group events with similar polarities across the network and calculated the associated focal mechanisms. They found that the results are consistent with the results obtained by Waite and Smith (2002) [Shelly and Hardebeck, 2019].

In 2020, Russo et al. relocated 10,201 earthquake hypocenters that occurred at the Yellowstone volcanic plateau between 2010 and 2016. They also calculated 224 new well-constrained, double-couple focal mechanism solutions and the stress field of this region. As a result, the revealed a σ3 orientation that trends NE-SW to ENE-WSW and is consistent with the regional extension [Russo et al., 2020].

1.3 Seismicity

The Yellowstone region is one of the most seismically active areas of the western US. The largest historic earthquake in the contiguous US occurred 25 km northwest of the Yellowstone caldera. The Hebgen Lake earthquake broke along a pair of west-trending

normal faults totaling 40 km in length with up to 5.7 m of slip [Smith et al., 2009]. The most seismically active area is to the north of the caldera between Hebgen Lake and Norris Junction. The events are usually scattered within and south of the caldera except for small clusters of events on the SW caldera boundary, south of Old Faithful and beneath Yellowstone Lake [Smith et al. 2009; Farrell et al.,2009; Waite and Smith, 2004]. The ML6.1 Norris Junction earthquake in 1975 was also the largest recorded event to occur within the Yellowstone caldera [Smith et al. 2009]. Figure 1-1 shows the distribution of the earthquakes relocated for this study and Figure 1-2 shows the depth distribution.

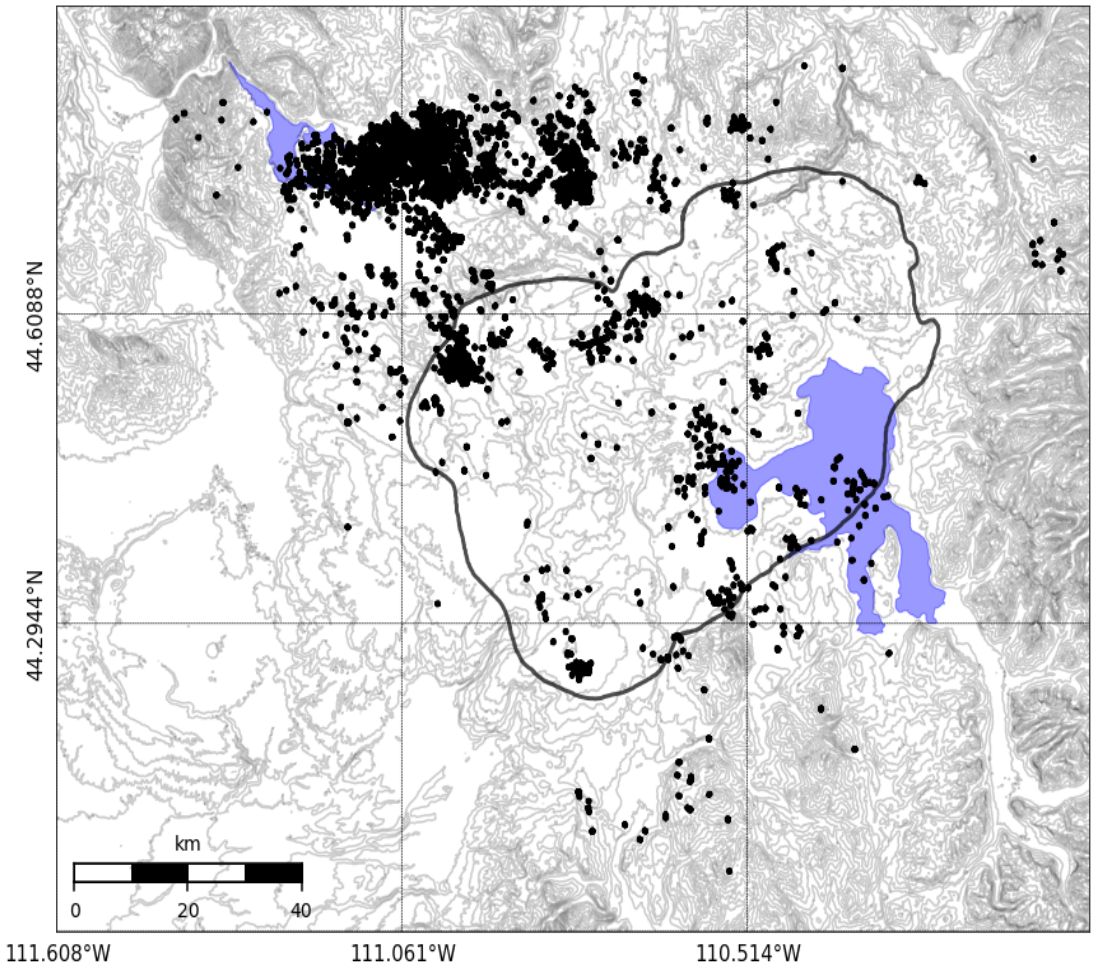

Figure 1-1: Relocated earthquakes used in this study. Between January 2010 and March 2021.

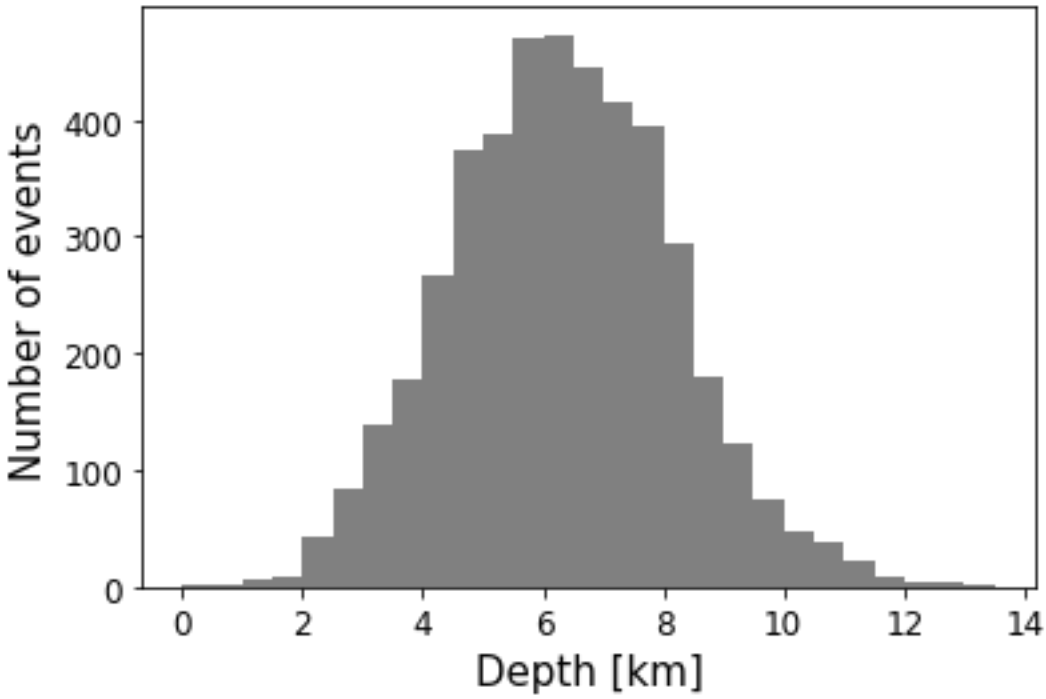

Figure 1-2: Depth distribution of the events used in this study.

2 Yellowstone: Motivation and objectives

There are several scientific motivations to study the Yellowstone Plateau. Firstly, this region is one of the most seismically active areas in the contiguous United States. According to the United States Geological Survey (USGS) information, one of the regional faults associated with this tectonic system triggered a devastating Mw 7.3 earthquake in 1959 that killed 28 people and caused $11 million in damage. Although a large volcanic eruption is not very likely, some of the associated risks include large and moderate earthquakes and hydrothermal explosions over the next few decades. And since thousands of visitors arrive every year at the Yellowstone National Park, it is crucial to understand the dynamics of this region to provide reliable information for hazard assessments.

This study aims to improve the locations of the existing catalog of events and calculate their focal mechanisms by using the P-wave first polarities and the S/P amplitude ratios to increase the number of solutions available. Another objective of this study is to calculate iterative joint inversions for stress from those focal mechanisms and look for spatial and temporal variations between January 2010 and March 2021. Ultimately, the main objective of this study is to improve our understanding of the state of stress in the Earth's crust at the Yellowstone Plateau.

3 Methodology

3.1 Seismic stations

We used 43 seismic stations distributed across the study area from 6 different networks to carry out this study. Table 3-1 summarizes the information of the station networks and the organization in charge. The group of stations used in this study included three-component broadband, short period, and borehole instruments. In addition, it also included some one-component stations. Figure 3-1 shows a map with the distribution of the station in the study area. We obtained the earthquake catalog from the University of Utah Seismograph Stations (UUSS). In addition, the seismic data obtained for this study are publicly available and can be accessed via the Data Management Center of the International Research Institutes for Seismology (IRIS DMC). Since this study comprises a period of more than eleven years, all the stations were not active simultaneously. Some of these stations went through instrument updates and changes. One of the most notorious changes was the name change of station H17A to YDD and its adoption in the WY network.

Table 3-1: Details of the stations and networks used in this study.

Network	Number of Stations	Operated by
Yellowstone National Park Seismograph Network (WY)	29	University of Utah
Plate Boundary Observatory Borehole Seismic Network (PB)	7	UNAVCO
Intermountain West Seismic Network (IW)	4	Albuquerque Seismological Laboratory /USGS
USArray Transportable Array (TA)	2	IRIS Transportable Array
United States National Seismic Network (US)	1	Albuquerque Seismological Laboratory /USGS
Montana Regional Seismic Network (MB)	1	Montana Bureau of Mines and Geology/Montana Tech

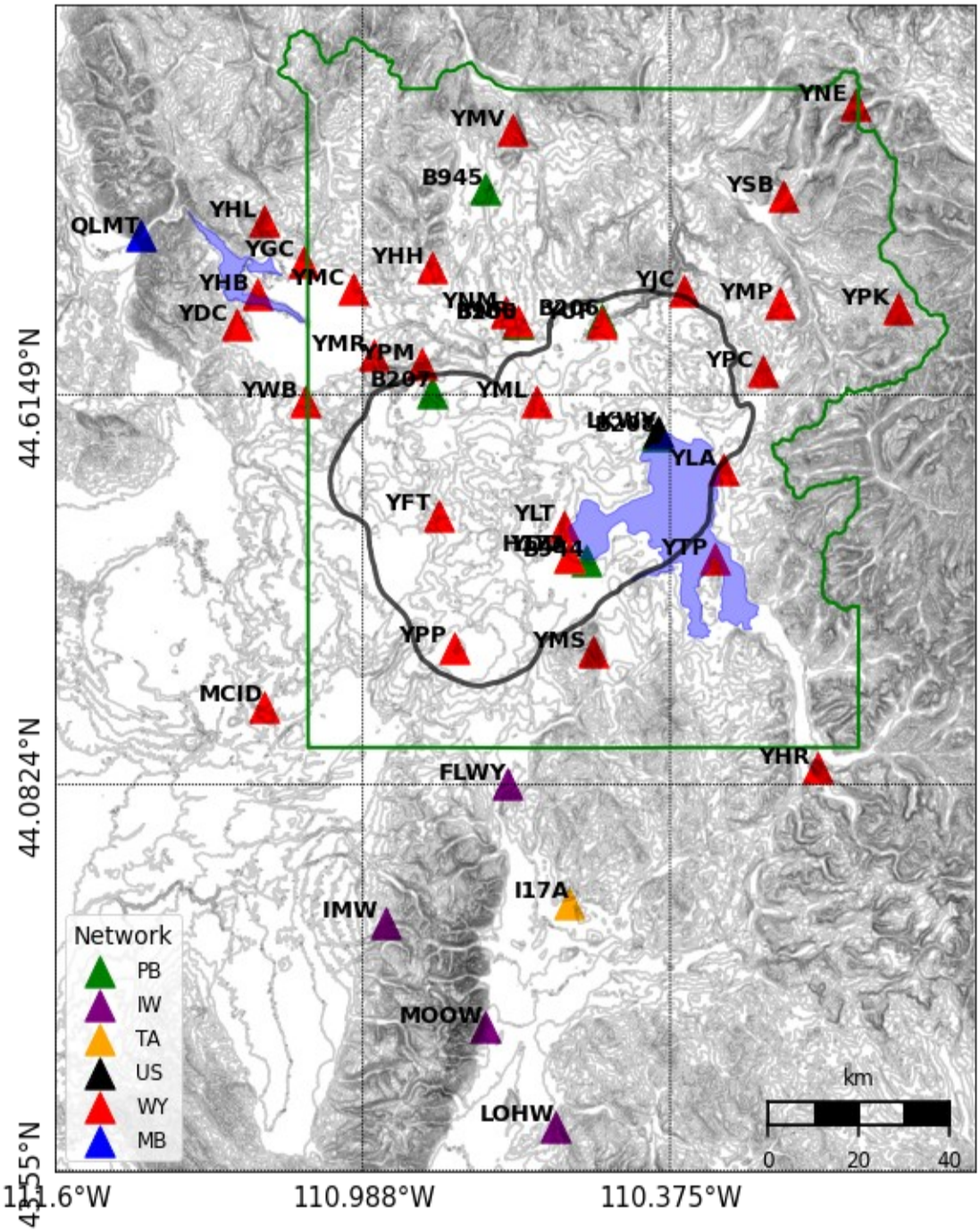

Figure 3-1: Seismic stations used in this study. The solid black line represents the third-cycle caldera defined by Christiansen (1984). The solid green line represents the limits of the Yellowstone National Park for reference.

3.2 Earthquake relocation: NonLinLoc

The earthquake location problem is a classical problem in geophysics, and generally, it is divided into two stages. First, we have the forward problem, where we compute the theoretical travel times. Second, we have the inverse problem where you search for the unknown parameters of the hypocenters. In earthquake location, the unknown parameters are the hypocentral coordinates and the origin time. In contrast, the observed data are the arrival times measured at seismograph stations and the theoretical travel times [Lomax et al., 2000; Russo et al., 2017; Wittlinger et al., 1993]. In order to relocate the earthquake catalog, we used the software package NonLinLoc [Lomax et al., 2000] following Husen and Smith (2004) and Russo et al. (2017).

The NonLinLoc (Non-Linear Location) package is a set of programs for velocity model construction, travel-time calculation, probabilistic, non-linear, global-search, and earthquake location in 3D structures. This software package was developed by Lomax et al. (2000) and uses the inversion approach proposed by Tarantola and Valette (1982) and the earthquake location methods proposed by Moser et al. (1992) and Wittlinger et al. (1993). To compute the theoretical travel times, NonLinLoc uses a three-dimensional velocity model to calculate the travel times between a station and all nodes of a spatial grid using the Eikonal finite-difference scheme of Podvin and Lecomte (1991). This program allows the formulation of inverse problems in a way that all the necessary constraints are satisfied. This method formulates the problem by using probability density functions (PDF) for data and parameters. Normalized and unnormalized PDFs express our knowledge about the values of parameters [Husen and Smith, 2004; Tarantola and Valette, 1982].

NonLinLoc offers three different ways to calculate the PDF. First, via a Metropolis-Gibbs sampling algorithm performing a directed random walk within a spatial volume to obtain a set of samples that follow the PDF. Second via an Oct-Tree Importance sampling algorithm; and third via a grid-search using nested grids [Husen and Smith, 2004; Lomax et al., 2000; Russo et al., 2017]. For the relocation of this study, we used the Oct-Tree algorithm option because it provides a more accurate and reliable mapping of the PDF. In

addition, some of the benefits of using this selection include higher speed than grid-search and greater simplicity since it only requires few initial parameters [Husen and Smith, 2004; Lomax et al., 2000].

We obtained the earthquake catalog from the University of Utah Seismograph Stations (UUSS). This catalog contained information for 18,940 events that occurred in the Yellowstone area between January 2010 and March 2021. This information included the location and origin time for all the events. It also contained P-wave first motions and the P and S-wave arrival times for all the stations used in this study that recorded a given event. First, this catalog was reformatted into a format readable by NonLinLoc by using Matlab scripts. Then, we used the program Vel2Grid to convert our tomographically determined three-dimensional P-wave velocity model developed by Farrell et al. (2014) into a 3D Grid file that contained velocity values. Next, we used the output file in the program Grid2Time to calculate the travel times between stations and all the nodes of a spatial grid. Several stations that lie outside the 3D velocity model were not considered for this calculation. Finally, we used the most recent output file and the reformatted catalog to run the NonLinLoc program. This process successfully relocated 15,806 events from the original earthquake catalog. The events that were lost were outside or near the edge of the 3D model grid so did not have travel times to a sufficient number of stations.

3.2.1 Best data selection

After the relocation process, we used several parameters to obtain a subset of best quality relocated earthquakes. To do this, we followed the definition of quality classes for earthquake locations proposed by Husen and Smith (2004). The authors defined four different quality classes from A to D, and for this study, we only considered events with quality class A. Table 3-2 summarizes the selection criteria used for the selection of the best subset of data.

Table 3-2: Selection criteria used for best data selection.

Selection criteria	Value
Minimum number of observations (P+S)	8
Azimuthal gap	< 180 degrees
Ratio of the distance to the nearest station	depth < 2
DIFF	< 500 m
Average error	< 2 km
RMS residual	< 0.5 sec

The first parameter was related to the number of observations. In general, as the number of observations increases, the earthquake locations will improve. Thus, we only included events with eight or more observations. Furthermore, good azimuthal coverage is crucial for improving the horizontal position of the event. In this case, we only accepted an azimuthal gap lower than 180°. In addition to this, the lack of nearby stations could result in a poorly constrained focal depth. For this reason, we established that the ratio of the distance to hypocentral depth could not exceed 2.

The parameter DIFF corresponds to the difference between the maximum likelihood and the expectation hypocenter locations. In this case, it was defined to be lower than 0.5 km. The average error is the average length of the three axes of the 68% error ellipsoid. Finally, since large residuals could indicate a problem with the arrival times, we only accepted an RMS residual lower than 0.5 sec. Based on all of the selection criteria, we obtained a subset of 7735 relocated events, and we proceeded with the calculation of the focal mechanisms for this subset.

3.3 Focal mechanisms calculation: HASH

Focal mechanisms of earthquakes represent the fault orientation, type, and slip direction for a point source. These mechanisms can provide critical information about the

faulting process and the stress field in which the earthquakes occur. They are computed using different techniques and data sets, such as P wave first-motion polarities, S wave/P wave amplitude ratios, and inversion of full waveforms. The methodology selection depends on data availability and the study purpose [Hardebeck and Shearer, 2002; Hardebeck and Shearer, 2003; Lin and Okubo, 2016]. For relatively large events, the focal mechanisms can be obtained through the inversions of full waveforms and geodetic observations. Unfortunately, for most relatively small earthquakes, it is not possible to apply these techniques. Some of the reasons include the difficulty in modeling the relatively high-frequency signals and the low amplitudes of the relatively small earthquakes. Despite the difficulty of constraining mechanisms of small events, these events could reveal crucial information for characterizing regional tectonics and constraining stress orientations because they occur much more frequently than large earthquakes [Hardebeck and Shearer, 2003]. For this reason, it is critical to use alternative ways of obtaining the fault-plane orientations and the slip directions.

HASH is a Fortran program designed to produce stable, high-quality focal mechanisms. The program HASH provides more stable solutions given the various sources of uncertainty that could exist, such as possible errors in the polarity observations, the imperfect knowledge of the seismic velocity structure, or errors in the assumed earthquake location [Hardebeck and Shearer, 2002]. This method was developed by Hardebeck and Shearer (2002) to calculate focal mechanisms by using the P wave first motion polarities. Later in 2003, it was updated to include S-wave/P-wave amplitude ratios in the focal mechanism calculation [Hardebeck and Shearer, 2003].

The P-wave first-motion focal mechanism determination problem can be separated into three stages. First, we have the polarity estimations (compressional or dilatational) that are obtained by using seismograms at each station. Second, we can get the angle at which the ray leaves the source, also called the takeoff angle, from the velocity model and the source and station locations. Then, by using the azimuth and the takeoff angles, we can determine the position for each station on the focal sphere for each observation. Finally, we have the optimal selection of nodal planes where we selected a focal mechanism that

best separates the regions of compressional and dilatational first-motion observations [Hardebeck and Shearer, 2002; Shelly et al., 2016].

Including S/P amplitude ratios has some advantages over simply using P-wave first motions. First, the number of observations per earthquake is increased. Second, these amplitudes have a range of values that could be used to constrain the location of a station more precisely on the focal sphere compared to the P-wave first-motion information. In general, the amplitudes of the P-wave are large near the P and T axes and small near the nodal planes. In the case of the S-wave, the amplitudes are large near the nodal planes. Thus, systematic variations in S/P amplitude ratios are predictable for a given focal mechanism [Hardebeck and Shearer, 2003; Shen et al., 1997].

We used two different approaches to calculate the focal mechanisms of the relocated events. For the first calculation, we only used the P-wave first-motion polarities included in the relocated catalog of earthquakes. We used the first-motion polarities in the second approach, but we also included the S-wave/P-wave amplitude ratios in our calculation.

3.3.1 P-wave first motion polarities only

The first polarities were obtained by observing at the P-wave first motion of every event to determine if the arrival was compressional (up) or dilatational (down). On the one hand, if the first arrival was compressional, the first motion was represented by one of the following characters: U, u, C, or +. On the other hand, if the first motion was dilatational, it was represented by: D, d, or -. If it was not possible to determine the first polarity, it was defined by '?'. All these polarities were picked manually by analysts from UUSS. During the installation and maintenance process, there is the possibility that a station was not installed correctly, and as a result, the polarity could be inverted. To address this problem, we double-checked the polarity of all the stations by using teleseismic earthquakes. Since teleseismic earthquakes occur far from our stations, they will arrive from the same direction

to all of them. We can take advantage of this because the P-wave first motion polarities must be the same at all stations. If this is not the case at a given station, it means that the polarity for that station is reversed. When we detected a station with a reversed polarity, we first determined the period in which they were reversed. Then, we corrected the polarities in the catalog before the focal mechanism calculation.

To do this, we selected teleseismic events with magnitudes greater than Mw 5.8 that occurred between January 2010 and March 2021at great-circle distances between 30° and 80° from the center of our study area defined at [Lat: 44.5°, Lon: -110.75°]. This yielded 71 events that met these criteria so that the time gap between earthquakes was not greater than 2~3 months. We got the data using automated Python scripts that request the seismograms and the seismic response files from the Incorporated Research Institutions for Seismology (IRIS) database. We downloaded 25 seconds of data for each station following the predicted arrival time of each event at all available stations only for the vertical component. We obtained the predicted arrival time by using the iasp-91 1D velocity model developed by Kennett and Engdahl (1991).

All the downloaded data underwent an essential preprocessing stage. First, we removed the seismic response, then we detrended and tapered the data. Next, to window the data, we used the estimated arrival time for the P-wave. Then, we resampled the data to 10 Hz and windowed the seismograms 5 seconds before and 15 seconds after the predicted arrival time. Finally, we filtered the data by using a frequency band between [0.5 - 5] Hz. After the preprocessing, we plotted all the seismograms for every event by the distance to the source. Then, we determined the polarities were correct by visual inspection.

After correcting our polarities by using Python codes, we created the input files required by HASH. These files have all the information for all the events and all the stations that recorded that event. The main file includes the first polarity, the azimuth, and the takeoff angle to each station. With all this information, it was possible to run the code HASH. We used the default parameters following Hardebeck and Shearer (2002). Finally, since some of the events obtained different solutions, we filtered the results to get a single

solution per event. To do this, we used the quality criteria summarized in Table 3-3, this is a modified criteria from the original criteria of the HASH program. If one event had more than one solution, we kept the one with the best quality, but if all the solutions had the same quality, they were filtered out. Finally, we plotted all the focal mechanisms using an open-source library called Pyrocko developed by Heimann et al. (2017).

Table 3-3: Quality criteria used for focal mechanisms.

Quality	Average misfit	RMS fault plane uncertainty	Station distribution ratio	Mechanism probability	Average log10(S/P) misfit
A	≤ 0.15	≤ 25°	≥ 0.5	≥ 0.8	≤ 0.25
B	≤ 0.20	≤ 35°	≥ 0.4	≥ 0.6	≤ 0.30
C	≤ 0.30	≤ 45°	≥ 0.3	≥ 0.5	≤ 0.35
D	maximum azimuthal gap ≤ 90°, maximum takeoff angle gap ≤ 60°				

3.3.2 P-wave first motion polarities and S/P amplitude ratios

This second approach used the same information as used before, plus the S/P amplitude ratios. HASH uses the amplitude ratios to improve the focal mechanisms; these ratios provide crucial information about the distance of the stations to the nodal planes. On the one hand, relatively low log(S/P) values are expected at stations that fall near the middle of a compressional or dilatational quadrant of the focal mechanism. On the other hand, stations falling near the nodal planes are expected to have a higher average log(S/P) [Hardebeck and Shearer, 2003]. This approach required additional input files, one with the S-wave, P-wave, and noise amplitudes and one with the station corrections.

3.3.2.1 Obtaining the amplitudes

To obtain the amplitudes, first, we preprocessed the data following a similar process as described before for the polarity reversal check. The only differences are the frequency band used to filter the data and the used windows of data. Some frequency bands were tested, and we did not observe important differences between them. So, we filtered the data using a frequency band between [1 - 12] Hz and rotated the horizontal component to the radial and traverse components. At this point, we also made sure that the horizontal components are correct. This test consisted of plotting the vertical and radial components together to determine if they were on phase or not and correct them if required. To do this, we used the same teleseismic earthquakes that we used for the reverse polarity check. This inspection is critical since we sum both components to obtain the amplitudes, and if the components are not in phase, the amplitudes could be underestimated.

In our catalog, not all the stations had an S-wave pick. And we decided to take two different approaches to see if it was possible to increase the number of S-wave picks for the focal mechanism calculations. We only used the S-wave arrivals times from the catalog for the first approach, and we used the windows shown in Figure 3-2 to obtain the amplitudes. Then we used the velocity a 1.65 Vp/Vs ratio estimated for the Yellowstone area [Husen et al., 2004; Farrell et al., 2014] to estimate the arrival times for the S waves. The difference between both windows is less than a second, and for this reason, we choose the second approach, and we increased the number of ratios from 16,752 to 36,295. This significant number of ratios allowed us to increase the number of focal mechanism solutions since, in both cases, we only accepted focal mechanisms with eight or more measurements combined between first polarities and ratios.

Figure 3-2: Windows used for amplitudes measurement. Example for station YMR. The blue lines represent the P and S picks, respectively. The first window is for the P noise, and it has a length of 1.5s. The second window is for the P amplitude, and it has a length of 0.45s. The third window is for the S noise, and it has 0.9 s. Finally, the last window is for the S amplitude, and it has 2s.

3.3.2.2 Obtaining the station corrections

The S/P amplitude ratios need to be corrected for site and path effects and also for path attenuation effects. It is necessary to assume that all station site effects are linear, so the correction is simply a scalar offset to the observed mean value [Hardebeck and Shearer, 2003]. The value of the empirical station correction was obtained for all the stations, following Shen et al. (1997). First, we established 72 intervals from 0 to 360 degrees to ensure an excellent azimuthal distribution at each station. Good azimuthal coverage is crucial to ensure that the data distribution will not be narrower than the predicted distribution. A good distribution also provides a relatively unbiased sampling of the focal sphere. We used the complete relocated catalog and only allowed a maximum of 8 events per interval. The available number of events for the different three-component stations ranged between 12 and 492. Figure 3-3 shows a map with all the events used for the stations with the maximum number of earthquakes, meaning an excellent azimuthal coverage.

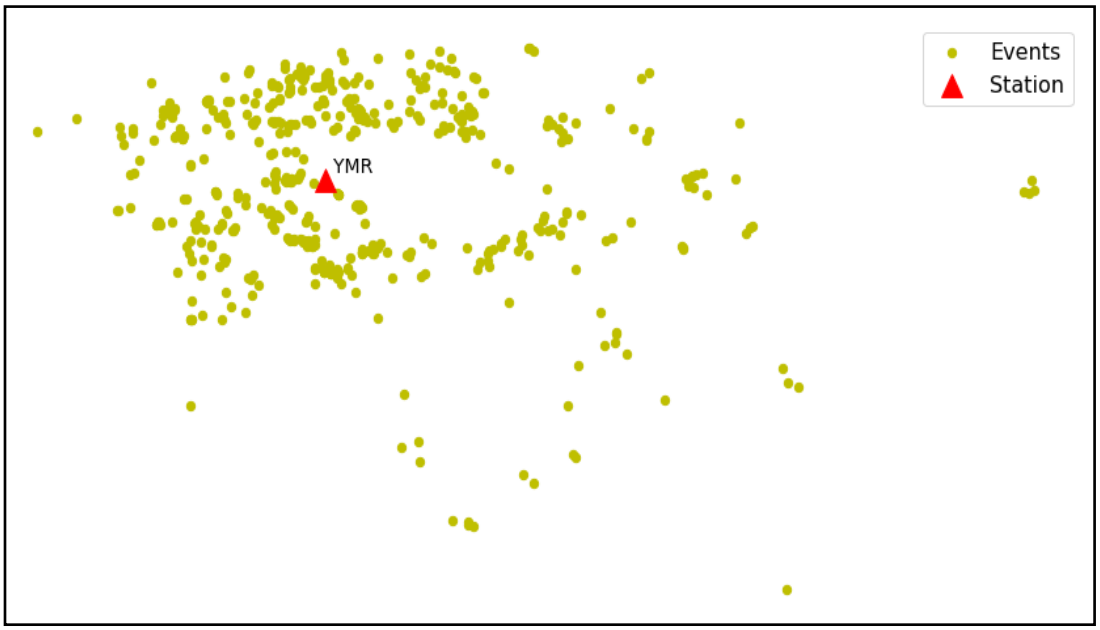

Figure 3-3: Azimuthal distribution of events that were used for calculating the station correction at station YMR (WY).

We obtained the observed distribution by using the S/P ratios for the selected earthquakes at a given station. Whereas the predicted distribution was obtained by using the following equations:

$$u_r = \frac{1}{4\pi\rho\alpha^3 r}\,\dot{M}\left(t - \frac{r}{\alpha}\right)\,\sin 2\theta\, cos\phi$$

The first term is an amplitude term, the second term is the seismic moment rate function, and the last term describes the P-wave radiation pattern.

$$u_\theta = \frac{1}{4\pi\rho\beta^3 r}\,\dot{M}\left(t - \frac{r}{\beta}\right)\,cos2\theta\, cos\phi$$

$$u_\phi = \frac{1}{4\pi\rho\beta^3 r}\,\dot{M}\left(t - \frac{r}{\beta}\right)\,(-cos\theta\ \sin\phi)$$

The first terms are again amplitude terms, the second term is the seismic moment rate function, and the last term describes the S-wave ration pattern in both components. These equations allow the calculation of the distribution for uniform sampling of the focal sphere [Stein and Wyssesion, 2009]. Since we needed the ratios, it was necessary to solve the equations, and we obtained the following equation:

$$\frac{\sqrt{{u_\theta}^2 + {u_\phi}^2}}{u_r} = \left(\frac{\alpha}{\beta}\right)^3 \frac{\sqrt{(cos2\theta\, cos\phi)^2 + (-cos\theta\ \sin\phi)^2}}{\sin 2\theta\, cos\phi}$$

In this equation, the term α/β is the Vp/Vs velocity ratio, and the other term describes the radiation pattern for the different components. To obtain our predicted distribution, we used 500,000 random combinations of ϕ and θ (Figure 3-4A). Figure 3-4B shows the observed distribution of one of the stations used in this study. Finally, the station corrections were obtained by shifting the mean of the observed distribution to match the mean of the theoretical distribution for all the stations.

After creating all the input files, we needed to modify the Vp/Vs velocity ratio in the HASH code to match our study area's ratio. Table 4-3 summarizes the parameters used for this calculation. These parameters were selected by following Hardebeck and Shearer (2003). Finally, since some of the events obtained more than one solution, we filter the results to keep only one solution per earthquake before running the inversion.

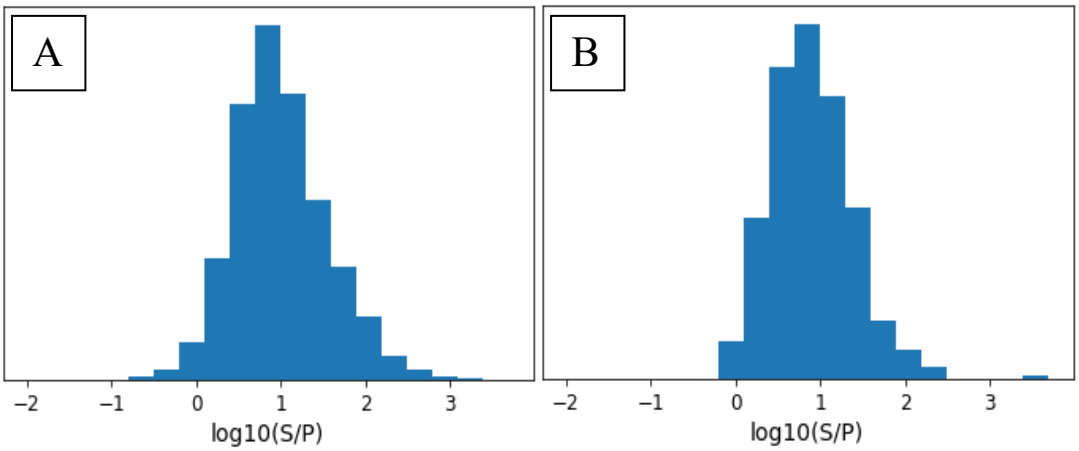

Figure 3-4: Predicted and observed theoretical distributions. A: Predicted distribution. B: Observed distribution for station YMR.

Table 3-4: Parameter used for focal mechanism calculation in HASH

Description	HASH parameter	Value
Minimum number of data	npolmin	8
Grid search angle for focal mechanism	dang	5
Number of trials	nmc	30
Maximum focal mechanism outputs	maxout	300
Minimum allowed signal-to-noise ratio	ratmin	3
Fraction of impulsive polarities assumed bad	badfrac	0.1
Assumed noise in amplitude ratios, log10	qbadfac	0.3
Maximum allowed epicentral distance	delmax	120 km
Angle for computing mechanism probability	cangle	45
Probability threshold for multiples	prob_max	0.25

3.4 Stress inversion: STRESSINVERSE

Focal mechanisms could be used to run stress inversions and determine the stress field of a given area. These inversions use the fault orientation and the slip direction of a

group of focal mechanisms to determine the stress field present during the faulting process. However, there is a complication since focal mechanisms have two different nodal planes, and most of the time, we do not know which nodal plane is the actual fault. Therefore, if the auxiliary nodal planes and the faults are interchanged, the stress inversions can produce inaccurate results [Vavryčuk, 2014].

Different methods and modifications for determining tectonic stress from focal mechanisms have been proposed [e.g., Angelier (2002); Arnold & Townend, 2007; Gephart & Forsyth, 1984; Lund & Slunga, 1999; Maury et al., 2013; Michael, 1984]. Usually, these methods make three critical assumptions; first, they assume that the tectonic stress is homogeneous in the region. The second assumption states that earthquakes occur on pre-existing faults with varying orientations. Finally, the third assumption says that the slip vector points in the direction of shear stress on the fault. If these assumptions are satisfied, the inversion methods determine three angles representing the directions of principal stresses, $\sigma 1$, $\sigma 2$, $\sigma 3$, and the ratio R which relates the relative amplitudes of the principal stresses [Gephart & Forsyth 1984; Vavryčuk, 2014].

STRESSINVERSE is a Matlab software package for an iterative inversion for stress and fault orientations from focal mechanisms. This package was developed by Vavryčuk (2014). The inversion routines of this program are based on a method proposed by Michael (1984, 1987). The fault orientations are obtained by applying the fault instability constraint proposed by Lund & Slunga (1999). The stress is calculated in iterations removing the necessity of knowing the fault plane.

To obtain the stress inversion results, we ran different inversions using different sets of data. For the first inversion, we used all the obtained solutions. Then, we divided our study area into 20 areas defined by an equally spaced grid to provide a starting point for defining areas of relatively homogeneous stress. We began with smaller areas and then

keep combining them to observe how the inversion results were changing. Finally, we defined 12 different regions using the stress direction as the main parameter (Figure 3-5).

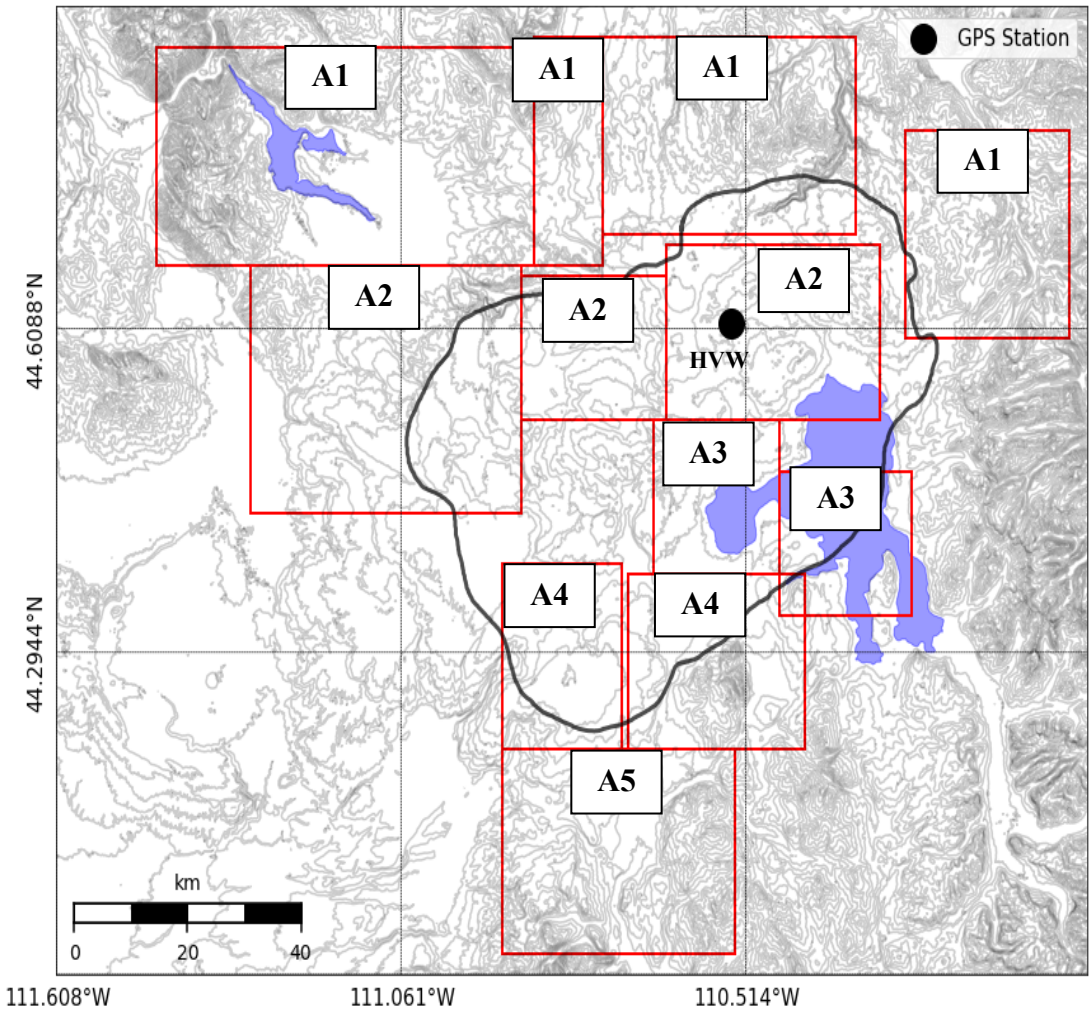

Figure 3-5: Areas defined for stress inversion. The black point represents the GPS station used to determine the periods of uplift and subsidence.

Finally, we used GPS data to establish three different periods to evaluate the temporal variation. We identified the episodes of uplift and subsidence determined to set the limits of the used periods. The first period goes from January 2010 until the first quarter of 2014. The second period is from 2014 to middle 2017, and the last period is from mid-2017 until March 2021 (Figure 3-6).

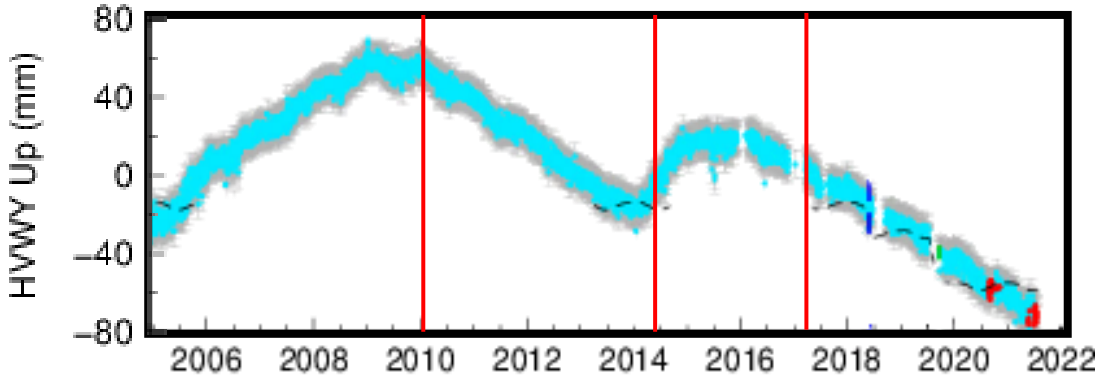

Figure 3-6: GPS data obtained from the USGS. This is the vertical component of the GPS station HVWY used to define the periods of subsidence and uplift. The solid red lines represent the limits of the defined periods.

We obtained two sets of inversions for each case, one using the complete catalog and the other only using the focal mechanisms with quality A, B, and C. In the next section, we present the results.

4 Results

4.1 First polarity only

HASH produces a single output file with all the solutions, and this file uses a single line per event. The information includes ID of the event, origin time, location, depth, the strike, dip, and rake of the focal mechanisms. We used this information to classify the faulting type as shown in Table 4-1. The output file also includes information about the uncertainty of both the fault and the auxiliary planes. In addition, it provides the values for the number of first polarities used in the calculation, the weighted percent misfit of first motions, the probability of the mechanism being close to the solution, the station distribution ratio, and the focal mechanism quality. We used the quality value assigned to each solution to define two different data sets. The first set contains all the obtained focal mechanisms and comprises 582 solutions (Figure 4-1). The second subset includes 421 solutions with qualities A, B, and C only (Figure 4-2).

Table 4-1: Faulting mechanisms classification.

Faulting type	Rake
Normal	-135 < rake < -45 or 225 < rake < 315
Right lateral	135 < rake < 225 or -225 < rake < -135
Left lateral	-45 < rake < 45
Reverse	45 < rake < 135

Table 4-2 shows the number of solutions by quality category. Finally, table 4-3 summarizes the number of focal mechanisms by fault type, considering all the available solutions and only considering the solutions with quality A, B, and C.

Table 4-2: Number of solutions by quality category.

Quality	Number of solutions
A	6
B	182
C	233
D	161
Total	582

Table 4-3: Number of focal mechanisms by fault type.

Mechanism	Number of solutions all	Number of solutions only quality A, B, and C
Normal	248	186
Right lateral	321	228
Left lateral	3	2
Reverse	10	5
Total	582	421

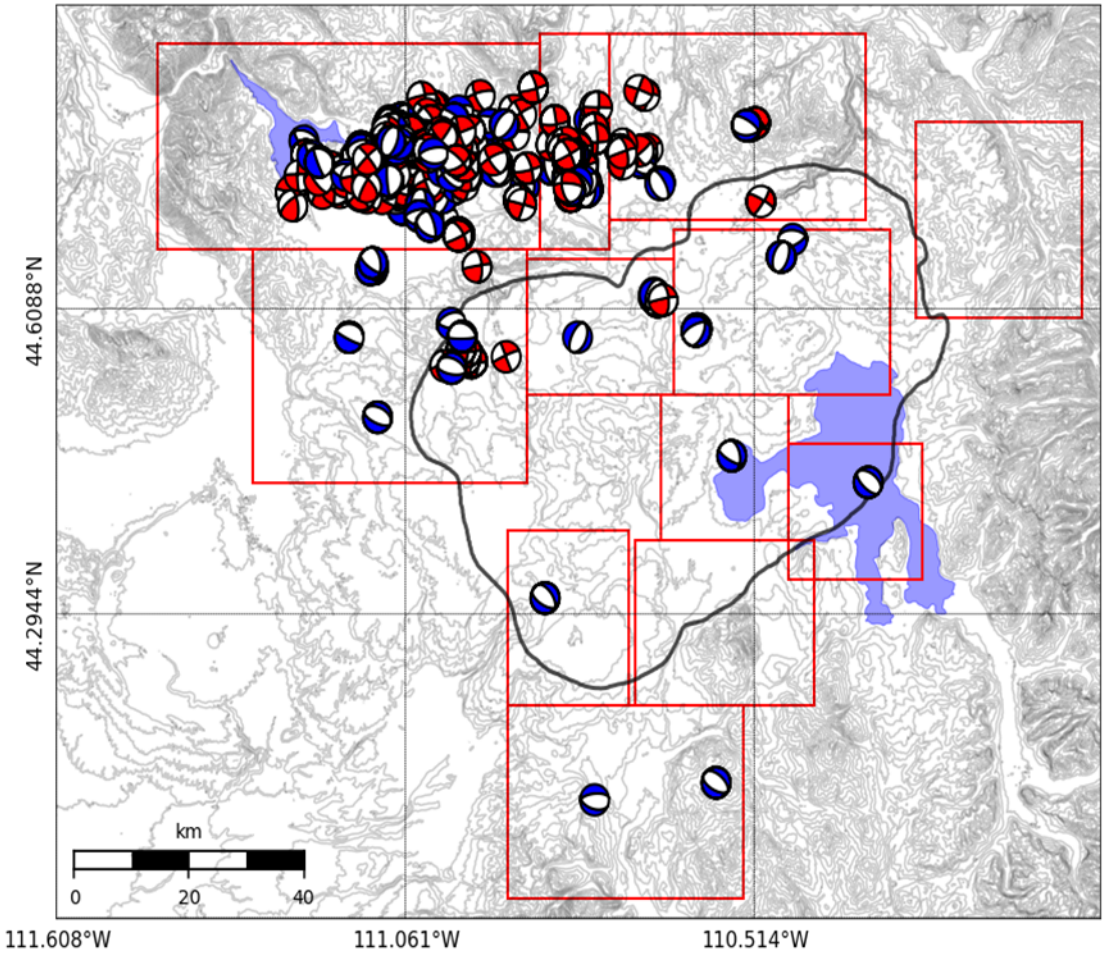

Figure 4-1: Focal mechanisms obtained by using only the P-wave first polarities. Red represents right lateral mechanisms, and black represents left lateral mechanisms. Blue represents normal faulting, and green represents reverse faults. The red rectangles represent the areas defined for the stress inversion.

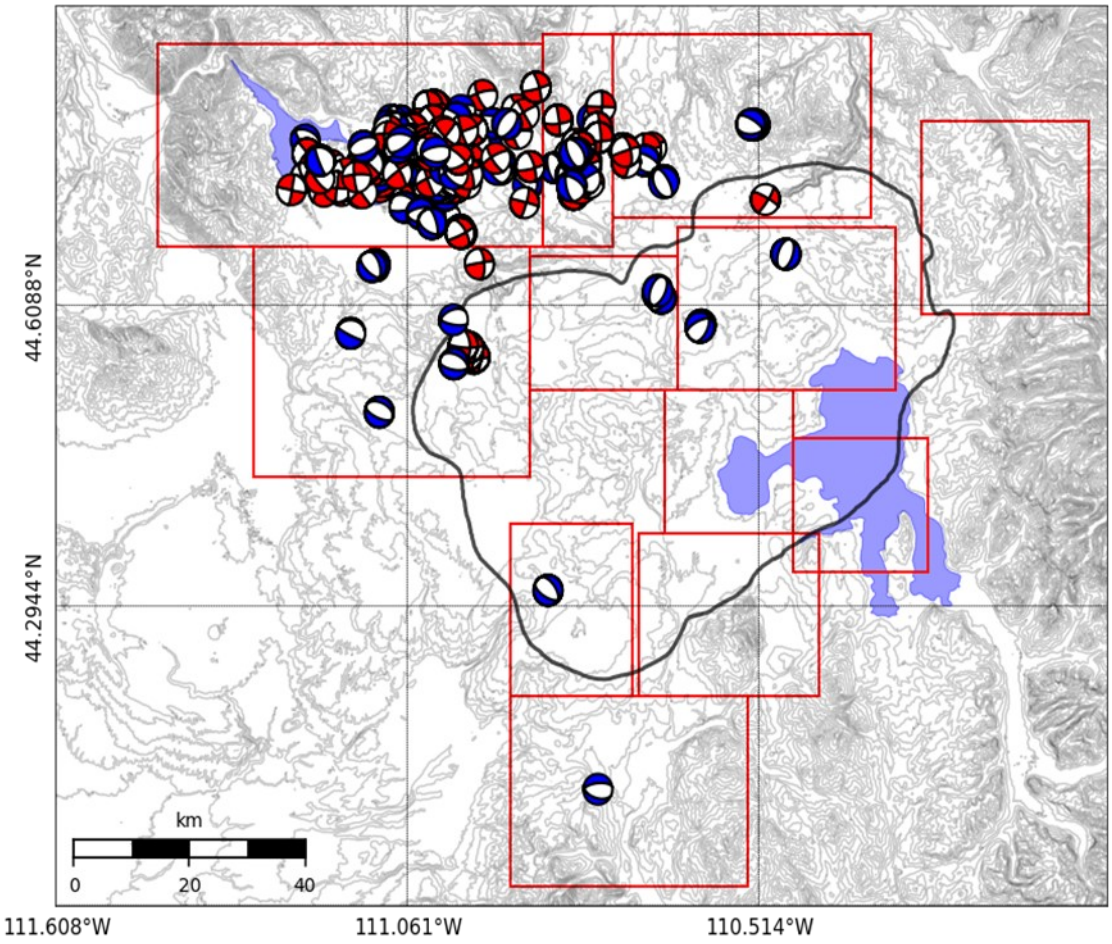

Figure 4-2: Focal mechanisms with quality A, B and C obtained by using only the P-wave first polarities. Red represents right lateral mechanisms, and black represents left lateral mechanisms. Blue represents normal faulting, and green represents reverse faults. The red rectangles represent the areas defined for the stress inversion.

We selected one focal mechanism per quality category to illustrate the differences between them. Tables 4-4 and 4-5 show details of the four chosen solutions, and Figure 4-3 shows the focal mechanisms, including the stations used in the calculation.

Table 4-4: Details of the four chosen solutions, one per category.

ID	Yr	Mo	Day	H	Min	Sec	Lat	Lon	Dep	Strike	Dip	Rake
6317	18	8	10	16	58	33.7	44.804	-110.98	6.7	111	20	-103
7584	20	11	25	2	14	40.45	44.773	-111.07	4.6	59	59	-114
7722	21	2	9	7	18	44.3	44.649	-111.12	5.8	133	52	-109
7688	21	1	22	17	21	4.43	44.780	-111.08	3.5	21	54	-91

Table 4-5: Additional information on the chosen focal mechanism.

ID	Fault plane uncertainty	Auxiliary plane uncertainty	Pol	Average Misfit	Qua	Mech probability	Station distribution
6317	22	25	13	0	A	87	55
7584	30	19	15	10	B	86	47
7722	34	33	17	27	C	58	48
7688	52	54	8	38	D	26	55

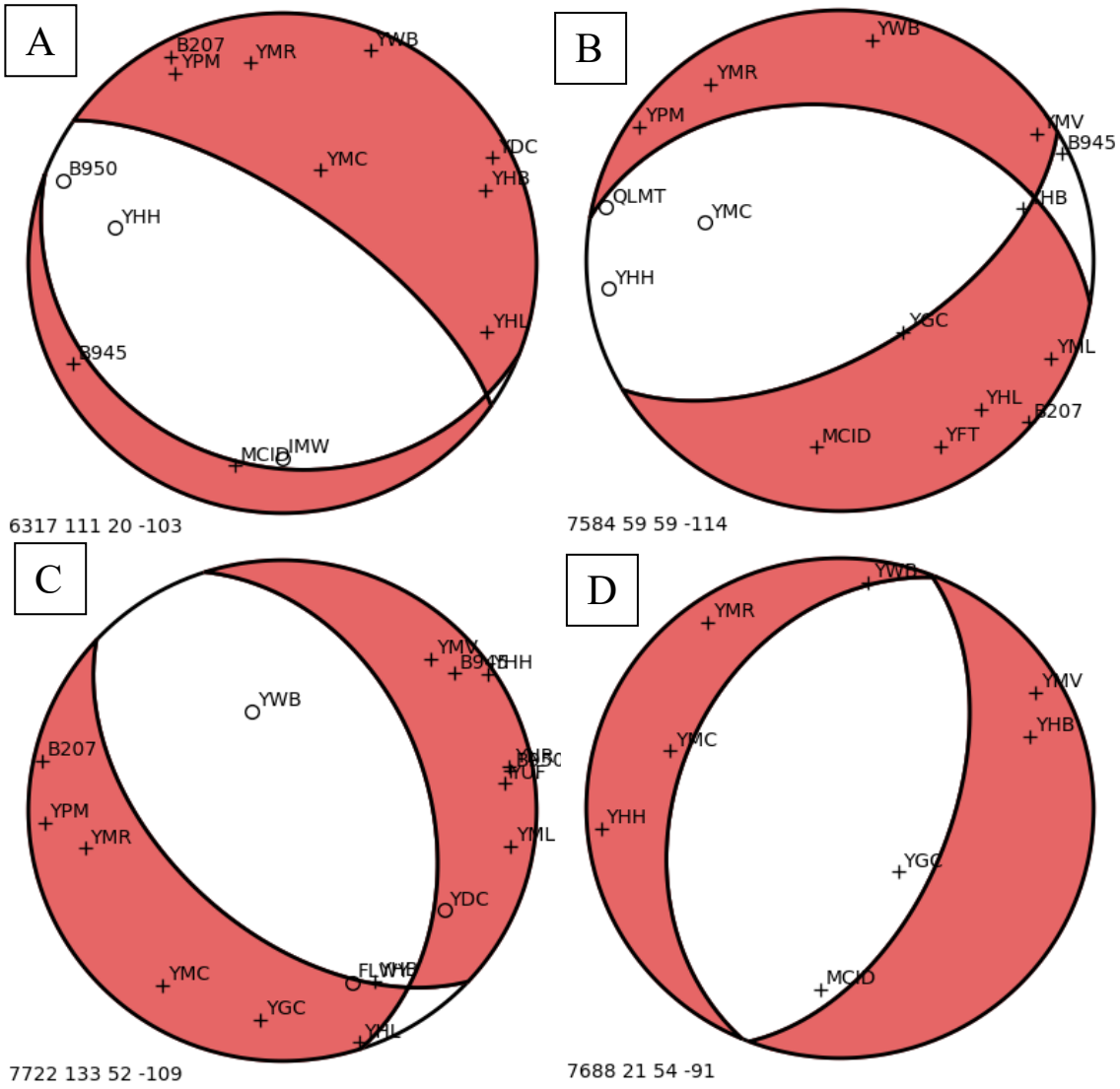

Figure 4-3: Focal mechanisms obtained using only first polarities. From category A To category D.

4.2 P-wave first motion and S/P amplitude ratios focal mechanisms

In this case, we also used the quality value assigned to each solution to define two different data sets. These results are the ones used in the stress inversions. The first subset includes 666 solutions with qualities A, B, and C only (Figure 4-4). The second one

contains all the obtained focal mechanisms and comprises 4500 solutions (Figure 4-5). Table 4-6 shows the number of mechanisms by quality category. Finally, table 4-7 summarizes the number of focal mechanisms by fault type, considering all the available solutions and only considering the solutions with quality A, B, and C.

Table 4-6: Number of solutions by quality category.

Quality	Number of solutions
A	15
B	253
C	434
D	3798
Total	4500

Table 4-7: Number of focal mechanisms by fault type.

Mechanism	Number of solutions all	Number of solutions only quality A, B, and C
Normal	1532	308
Right lateral	2275	288
Left lateral	111	32
Reverse	582	74
Total	4500	702

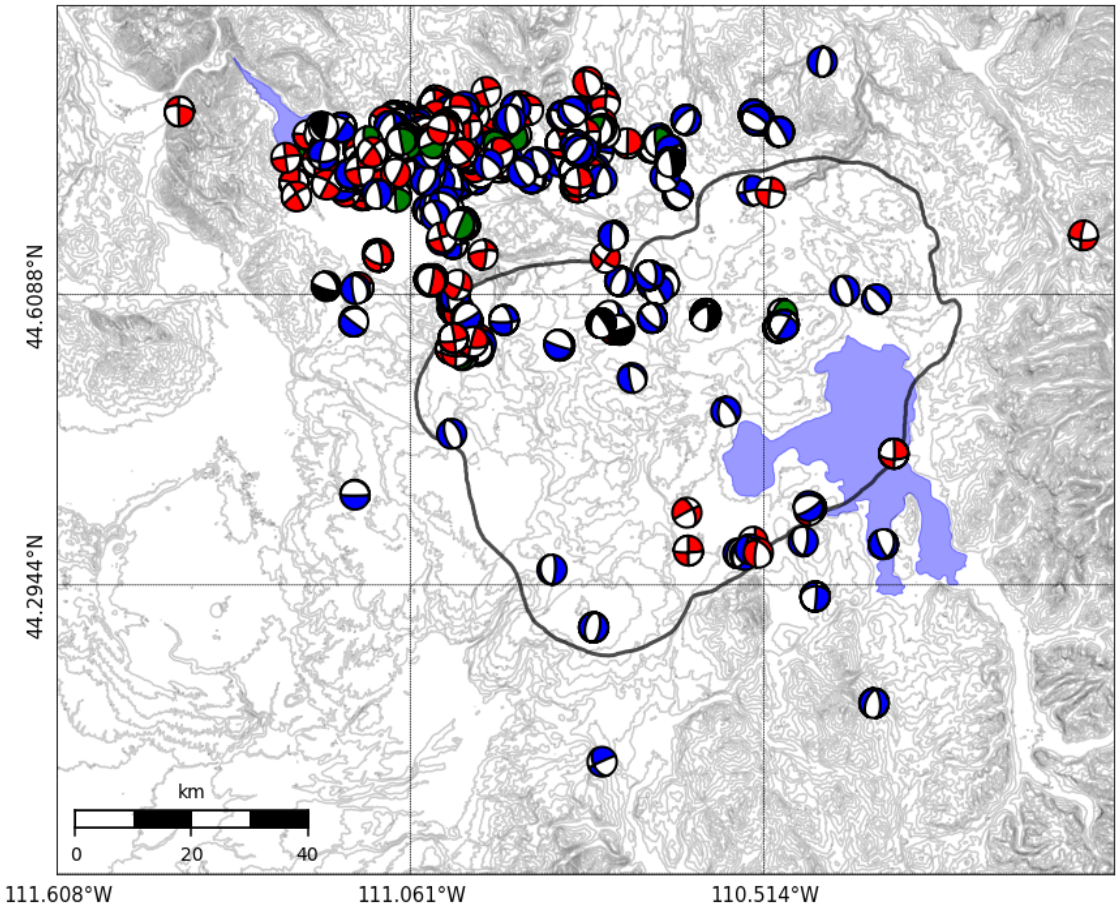

Figure 4-4: Focal mechanisms with quality A, B, and C obtained by using the P-wave first polarities and the amplitude ratios. Red represents right lateral mechanisms and black represents left lateral mechanisms. Blue represents normal faulting and green represents reverse faults.

In this case, we also selected four focal mechanisms, one per quality category. Tables 4-8 and 4-7 show details of the chosen solutions, and Figure 4-6 shows the focal mechanisms, including the stations used in the calculation.

Table 4-8: Details of the four chosen solutions, one per category.

ID	Yr	Mo	Day	H	Min	Sec	Lat	Lon	Dep	Strike	Dip	Rake
6758	19	7	15	7	54	57.1	44.797	-110.91	7.3	350	31	-94
5138	17	8	4	8	45	29.5	44.794	-111.08	4.7	17	71	-111
6358	18	9	11	13	30	54.5	44.860	-110.42	10.4	358	32	-99
6944	19	10	27	20	43	34.6	44.760	-111.80	2.8	223	50	-86

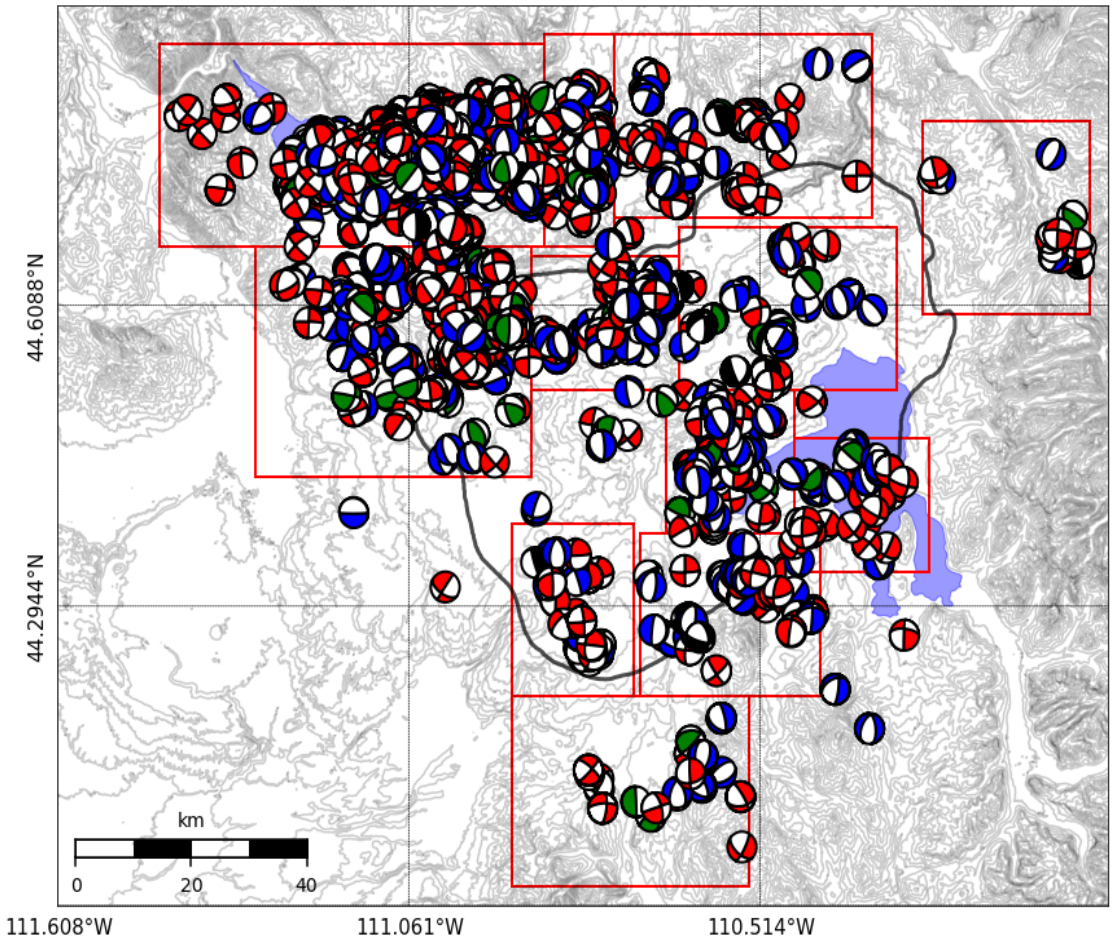

Figure 4-5: Focal mechanisms obtained by using the P-wave first polarities and the amplitude ratios. Red represents right lateral mechanisms and black represents left lateral mechanisms. Blue represents normal faulting and green represents reverse faults. The red rectangles represent the areas defined for the stress inversion.

Table 4-9: Additional details for the focal mechanisms.

ID	Fault plane uncertainty	Auxiliary plane uncertainty	Pol	Average Misfit	Qua	Mech prob	Sta dist	Rat	Ratio misfit
6758	18	20	17	13	A	96	45	7	38
5138	35	28	13	6	B	66	47	6	51
6358	46	38	18	7	C	52	50	14	52
6944	58	52	6	0	D	22	50	3	41

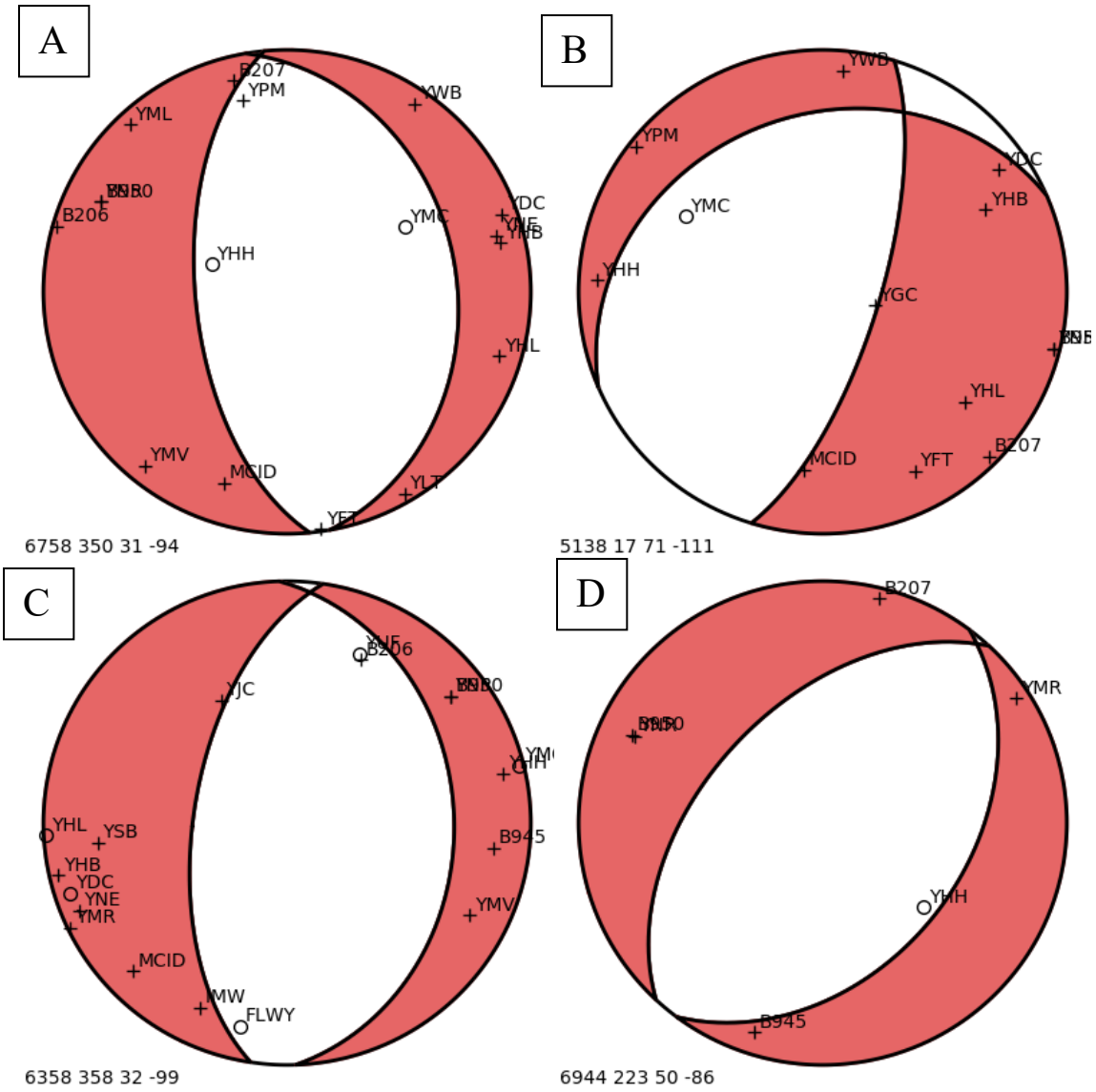

Figure 4-6: Focal mechanisms obtained using first polarities and amplitude ratios. From category A To category D.

Since we also included amplitude ratios in these calculations, we created plots with the amplitude ratios to evaluate them. Figure 4-7 shows an example designed for a focal mechanism with quality A and Table 4-10 shows the details of this event.

Table 4-10: Details of the focal mechanisms plotted to illustrate the amplitude ratios.

ID	Yr	Mo	Day	H	Min	Sec	Lat	Lon	Dep	Str	Dip	Rake
6317	18	8	10	16	58	33.7	44.804	-110.98	6.7	118	15	-103

Fault plane uncertainty	Auxiliary plane uncertainty	Pol	Average Misfit	Qua	Mech prob	Sta dist	Rat	Ratio misfit
14	24	13	11	A	94	55	5	37

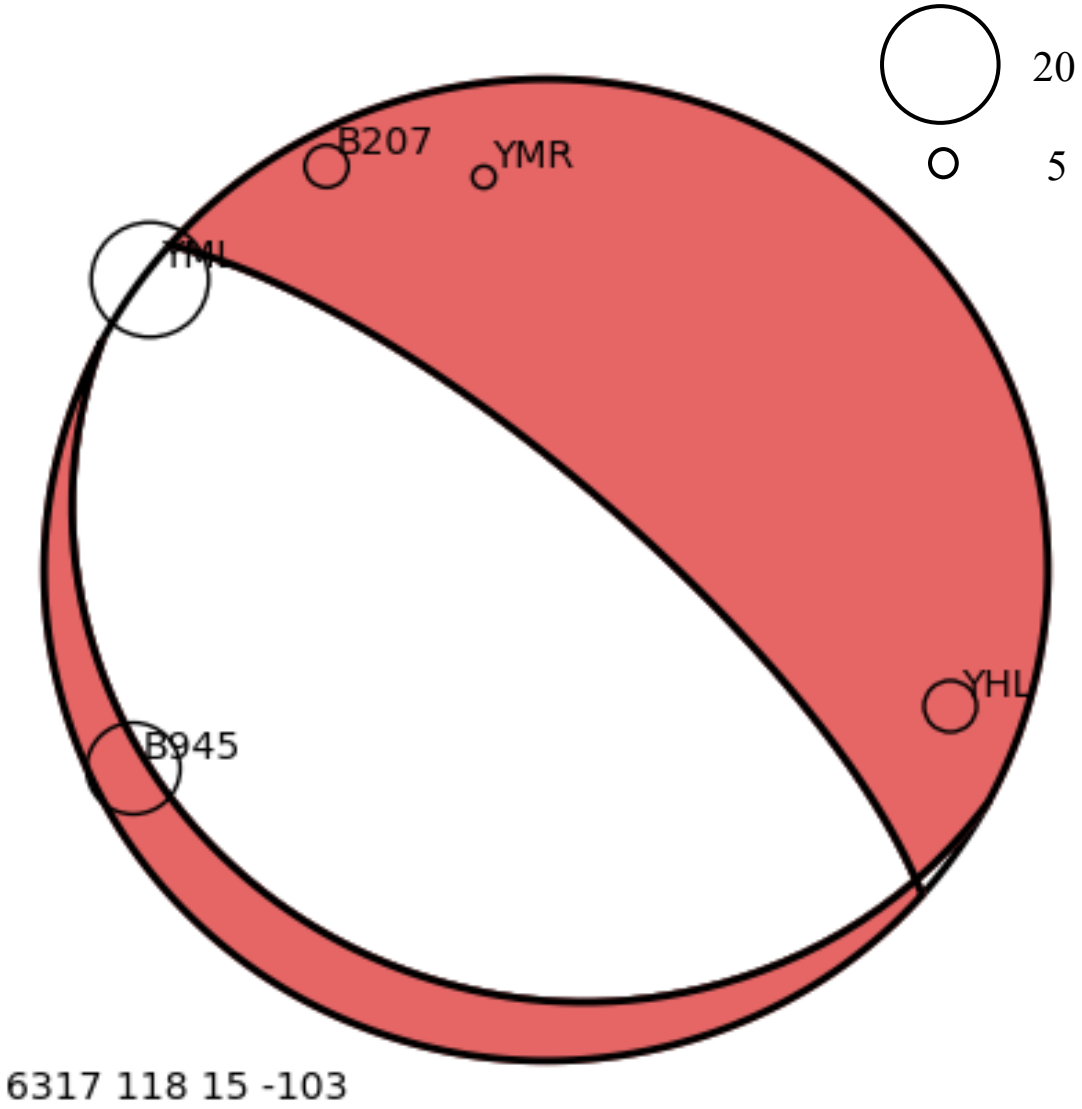

Figure 4-7: Focal mechanism plotted to illustrate the amplitude ratios. The size of the circles represent the amplitude ratio for each station.

4.3 Stress inversions

We used different sets of data for the stress inversion. However, we only used the results of the focal mechanisms obtained by using both the P-wave first motion polarities and the S-wave/P-wave amplitude ratios. Thus, the first set comprises all the solutions obtained in the different 12 defined areas. Figure 4-8 shows the resulting σ_3 directions for the first set of inversion, and table 4-11 summarizes the values of the principal stress directions for this set of inversions. There are only 3 areas with minimum principal stress direction greater than 10 from horizontal, and those are between 10 and 20 degrees. Table 4-12 shows the number of events by faulting type and the total number of solutions used in each inversion.

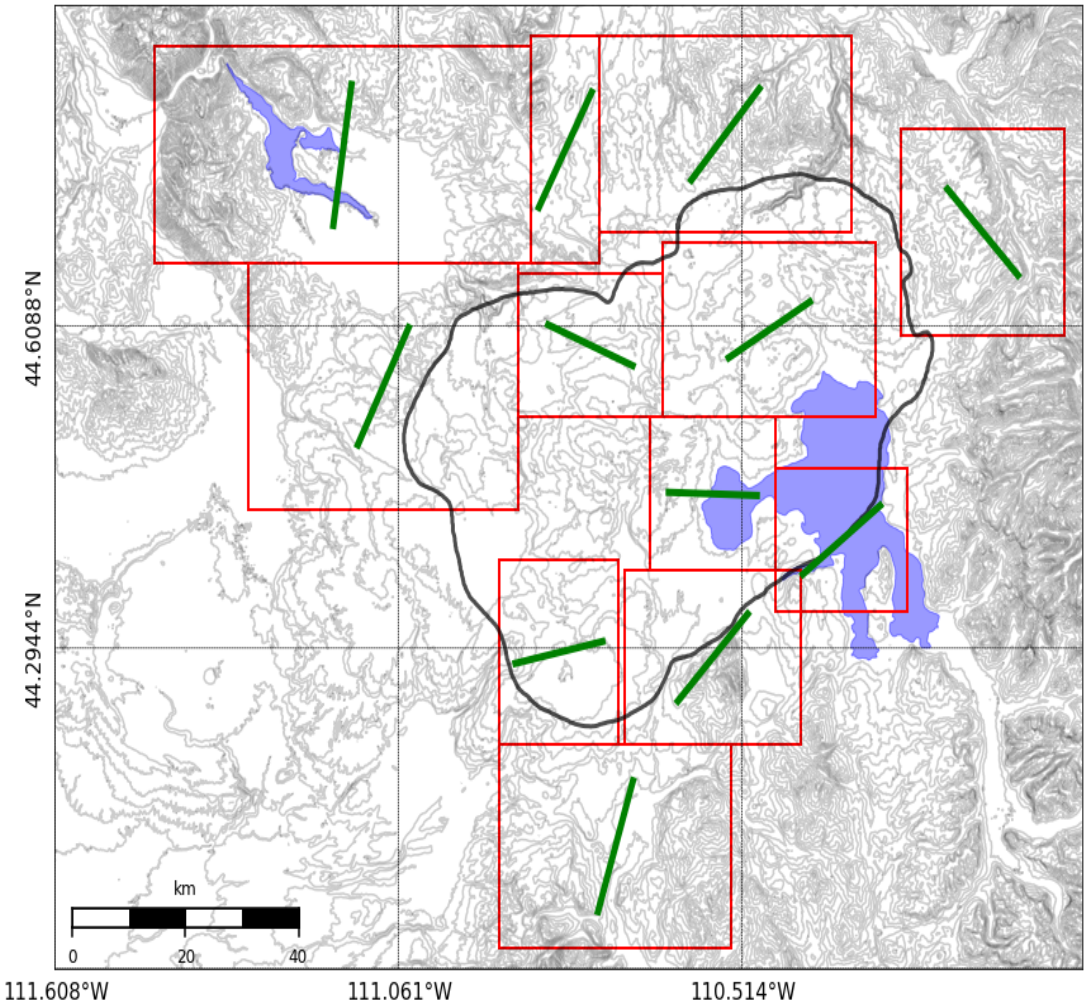

Figure 4-8: σ3 directions obtained for the selected areas by using all the solutions

Table 4-11: Results of the stress inversions using all the solutions available.

Area	σ_1	plunge	σ_2	plunge	σ_3	plunge
A11	281.08	63.756	102.21	26.24	11.989	0.4498
A12	173.03	82.845	306.52	4.9377	36.964	5.1658
A13	228.87	73.612	320.54	0.4922	50.688	16.38
A14	215.5	45.392	37.904	44.583	306.72	1.2005
A21	310.81	22.285	96.938	63.73	215.29	13.193
A22	318.06	79.762	197.29	5.2781	106.48	8.7474
A23	271.36	69.68	159.78	7.7536	67.148	18.662
A31	255.94	80.958	0.9053	2.3539	91.267	8.7256
A32	316.76	57.705	156.85	30.693	61.403	9.0796
A41	192.34	67.365	347.96	20.797	81.229	8.5399
A42	343.58	71.235	140.31	17.334	232.49	6.9676
A51	294.77	58.573	112.9	31.414	203.41	0.8315

Table 4-12: Number of events by faulting mechanism used in each inversion using all the solutions available.

Area	Normal	Right Lateral	Reverse	Left Lateral	Total
A11	890	1238	377	67	2572
A12	169	272	41	9	491
A13	39	49	12	4	104
A14	4	9	2	1	16
A21	196	523	97	12	828
A22	77	39	14	6	136
A23	27	16	9	4	56
A31	39	41	13	1	94
A32	22	24	4	0	50
A41	25	17	5	4	51
A42	31	30	2	3	66
A51	7	11	4	0	22

The second set comprises the solutions with quality A, B, and C obtained in the areas with more than 50 solutions. Table 4-13 shows the number of events by faulting type and the total number of focal mechanisms used in each inversion. In this case, only three

areas fulfilled this requirement, but we also included A22 in this set. Figure 4-9 shows the resulting σ_3 directions for the second set of inversion, and table 4-14 summarizes the values of the principal stress directions for this set of inversions.

Table 4-13: Number of events by faulting mechanism used in each inversion for best quality solutions.

Area	Normal	Right Lateral	Reverse	Left Lateral	Total
A11	221	178	57	20	476
A12	19	28	5	2	54
A13	15	2	1	2	20
A14	0	1	0	1	2
A21	20	45	3	3	71
A22	11	2	0	2	15
A23	10	0	1	1	12
A31	1	0	0	0	1
A32	3	2	0	0	5
A41	3	0	0	0	3
A42	2	1	0	0	3
A51	2	0	0	0	2

Table 4-14: Results of the stress inversions for best quality solutions.

Area	σ1	plunge	σ2	plunge	σ3	plunge
A11	290.32	65.845	115.92	24.053	24.988	2.0904
A12	126.799	39.531	311.13	50.388	218.55	2.130
A21	315.801	54.361	105.67	31.804	204.834	14.391
A22	4.7254	73.771	148.94	13.285	241.121	9.1513

5 Discussion

5.1 Focal mechanisms

The calculation of focal mechanisms by only using the P-wave first motion polarities resulted in 582 solutions. In comparison, the calculation where we included the amplitudes ratios resulted in 4500 solutions, which means that 3918 events reached the minimum number of observations allowed (8) and obtained a solution. The number of solutions with quality A went from 14 to 15. In the case of solutions with quality B, it decreased from 275 to 253. And finally, the number of focal mechanisms with quality C went from 178 to 434.

In general terms, the inclusion of the amplitude ratios helped increase the number of focal mechanisms and increase the number of best quality solutions. However, there were some cases when the quality of the solution decreased. For example, 5 out of 14 focal mechanisms with quality A when only using the polarities obtained quality B when we included the amplitude ratios. Figure 5-1 shows an example of one of these cases for an event in August 2017.

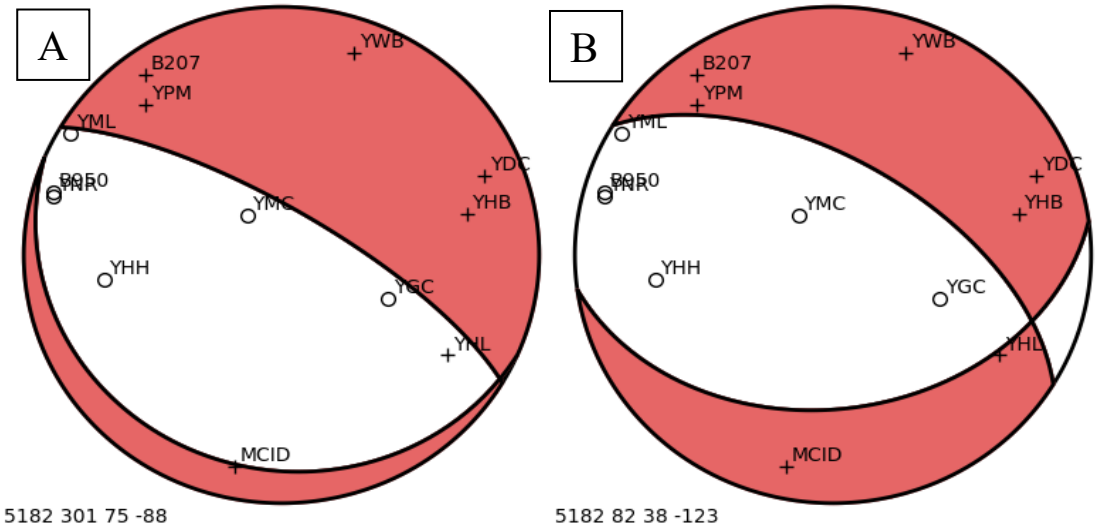

Figure 5-1: Differences between focal mechanisms obtained by using A: first polarities motions and amplitude ratios. B: first polarities motions only.

In the case of quality B, 99 solutions out of 275 remained with quality B, and 3 mechanisms improved to quality A. 83 solutions went from quality B to quality C, and 34 went down to quality D. Finally, 34 events obtained multiples with the same quality, and they were filtered out. For quality C, 53 events stayed in the same quality and 31 improved to quality B. Also, 37 mechanisms were downgraded to quality D. Finally, 313 events that obtained multiples with the same quality were discarded.

In the end, from the 467 mechanisms with quality A, B, and C obtained only using the polarities, 198 improved or stayed in the same category. But also, 154 events were downgraded to lower quality, and 115 were removed because they got multiples solutions with the same quality. One of the possible explanations is that the amplitude ratios of some of the stations were not correct. This problem could be caused by errors in the pick of the arrival times that led to wrong windows where the amplitudes were selected.

The new catalog where we included the amplitude ratios included 155 previous solutions with quality A, B, and C and created 547 new solutions with these qualities. In addition, 101 of those solutions came from previously calculated quality D mechanisms, and 446 came from events that did not obtain a solution when we used the first polarities only. Finally, 3683 new solutions with quality D were obtained from events that previously did not have a solution.

In summary, the addition of the amplitude ratios increased the number of solutions with the best quality. However, about 48% of the best quality solutions obtained with the first polarities only were downgraded or not considered when including the amplitude ratios. About 35% remained in the same quality, and only 17% improved. Finally, more than 58% of the best new quality solutions came from events with low quality or no solutions. This method proved to be efficient at improving the low-quality events, but it is inefficient at refining solutions with previously established good quality solutions.

Similar findings were reported in previous studies (e.g., Hardebeck and Shearer, 2003), where the authors computed focal mechanisms of aftershock sequences using amplitude ratios and first polarities. They concluded that the amplitude ratios might

improve poorly constrained mechanisms, but they are less useful in refining solutions that are already relatively well constrained.

5.2 Stress inversions

Crustal extension dominates the regional deformation pattern in the Yellowstone Plateau area. Extension directions are generally NNE-SSW immediately south of Yellowstone and E-W from the Teton Range south into southeastern Idaho [White et al., 2009]. North and west of Yellowstone, extension is dominantly NE-SW except in the vicinity of the 1959 Hebgen Lake earthquake where it is N-S or NNE-SSW [Smith et al., 2009].

Our results indicate variations of the stress field across the Yellowstone Plateau area. The set of inversions where we used all the available solutions show a rotation from NNE-SSW near the Hebgen Lake fault zone (area A11) to NE-SW near Norris Junction (area A13). The plunge values of σ_3 are close to 0, meaning that this direction is horizontal or near horizontal. These results are consistent near the Hebgen Lake fault zone with previously obtained stress fields orientations for this area determined by Waite and Smith (2004) and Russo et al. (2017) for the periods 1973-1998 and 1998-2010, respectively.

Area A14 shows an orientation that is very different from the rest of the study area. Since this inversion was carried out only with 16 events that are scattered within the area, we consider that these results are not reliable. Figure 5-2 shows the confidence of the principal axes for this area, where we can observe the significant uncertainty of these results. Area A51 presents an orientation consistent with the nearby areas. However, the inversion only included 22 focal mechanisms, and it is not considered very reliable.

Areas A32 and A42 located at the southeast boundary of the 0.64 Ma caldera near Yellowstone Lake show a similar orientation NE-SW. Area A41 is situated at the southwestern and indicates a direction ENE-WSW. Area A31, located west of Yellowstone

Lake, displays an E-W orientation. The northeast section of the caldera shows an orientation similar to A31, NE-SW. Area A21 is one of the areas with the most solutions, the orientation of this area is near NE-SW.

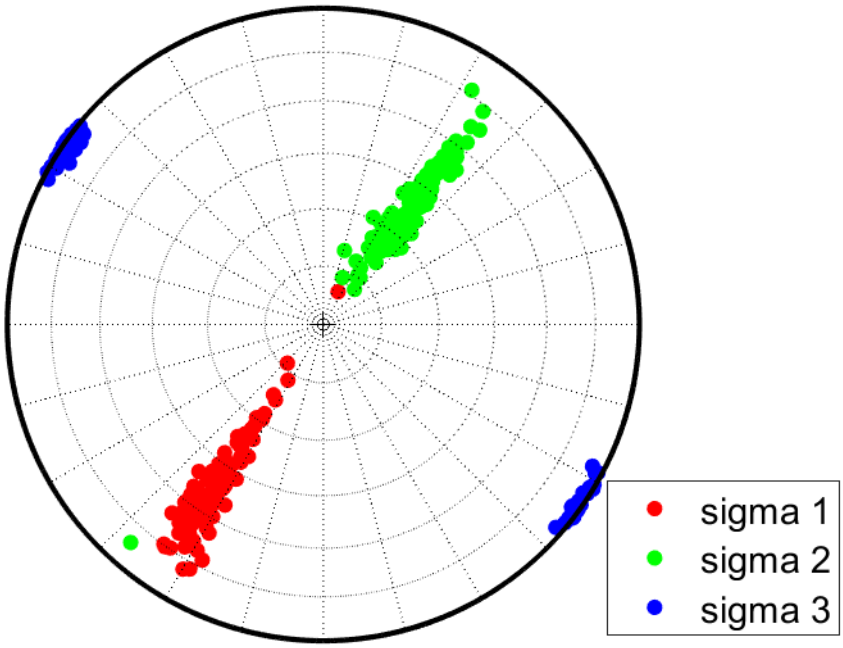

Figure 5-2: Confidence of the principal axes for area A14.

Area A22 shows a different direction compared to the rest of the areas. It shows an orientation WNW-ESE. To evaluate this result, we also ran a set of inversions using only solutions with qualities A, B, and C for areas A22, A11, A12, and A21. This new set of inversions revealed that A22 has an ENE-WSW orientation consistent with the nearby locations. Finally, we also ran inversion to evaluate the temporal variations. This evaluation was only possible for two areas because of the earthquake distribution through the years. Figure 5-3 shows the distribution of the seismicity through the years for areas A11 and area A22. Furthermore, Figure 5-4 displays the evolution of the principal directions in the periods of uplift and subsidence defined by using GPS data. We can observe the rotation of the principal axes between the different periods of uplift and subsidence.

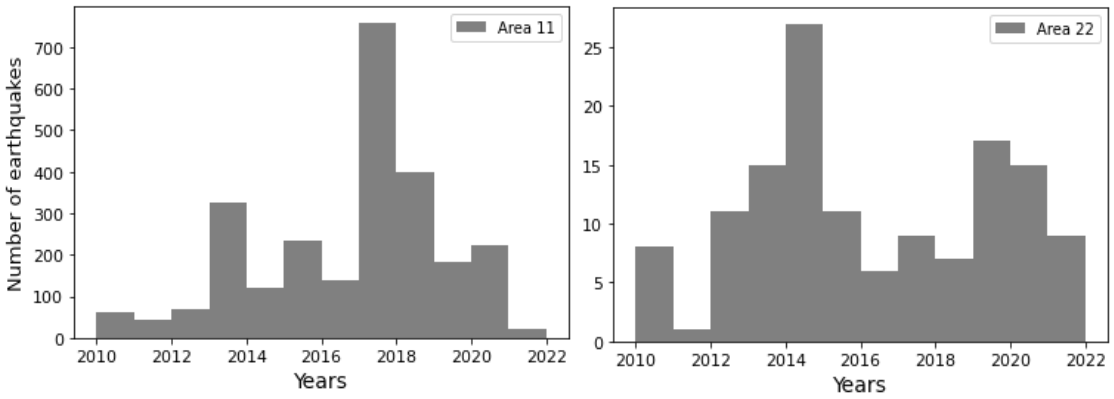

Figure 5-3: Distribution of the seismicity through the years for areas A11 and area A22.

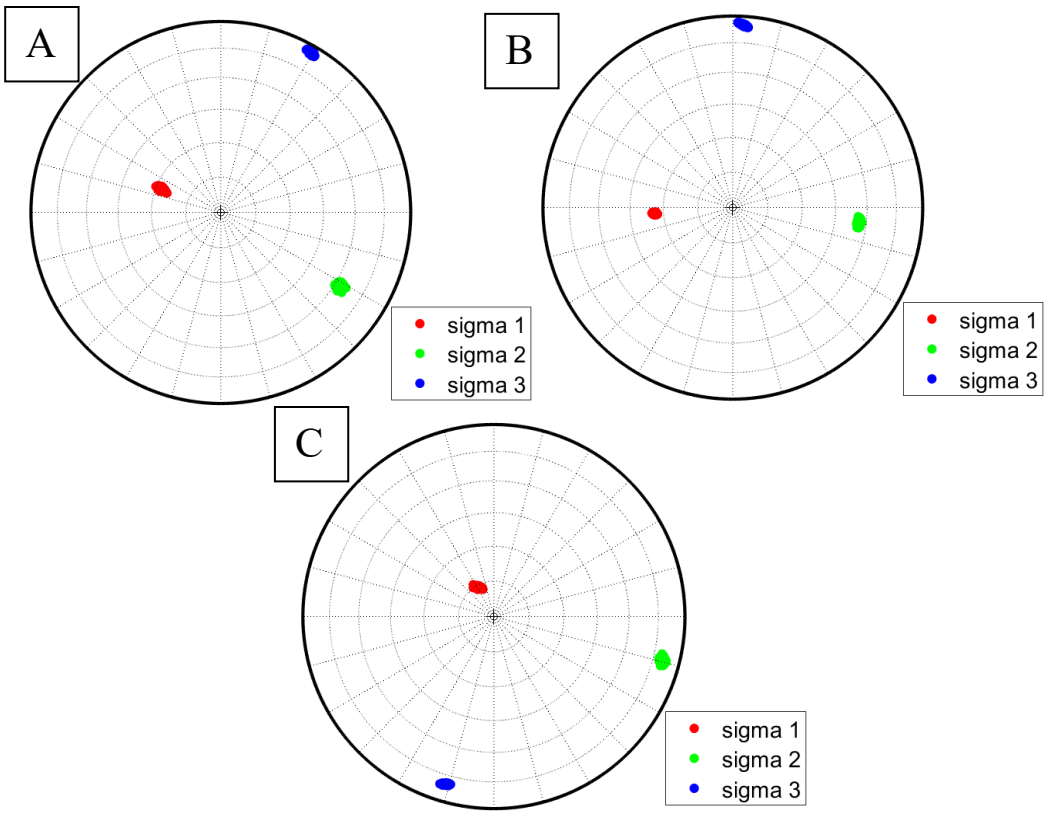

Figure 5-4: evolution of the principal directions in the periods of uplift and subsidence defined by using GPS data. A: between 2010 and 2014. B: between 2014 and 2017. C: between 2017 and 2021.

6 Conclusion

We conducted a comprehensive study of earthquake source mechanisms at Yellowstone using P-wave first motions and S/P amplitude ratios. We first relocated and filtered a catalog of 18,940 earthquakes between January 2010 and March 2021 recorded and analyzed by the specialist from the University of Utah Seismograph Stations (UUSS). We obtained 7735 high-quality relocated events, and we calculated focal mechanisms for all the events with more than eight observations using the analyst picked P-wave first motions. We obtained 582 solutions. We then added S/P amplitude ratios for those stations with horizontal components by extracting and analyzing data archived at the IRIS DMC. This calculation resulted in 4500 solutions after filtering the events with multiples solutions and the same quality. About half of the best quality solutions obtained with the first method were downgraded or not considered in the second approach. From these results, we can conclude that the inclusion of the amplitude ratios is efficient at improving the low-quality events and vastly increasing the overall number of solutions. Still, it is inefficient at refining solutions with previously established good-quality solutions.

Finally, we ran several inversions for stress and fault orientations from focal mechanisms by using different data sets to analyze the spatial and temporal variations of the stress field. We used 12 areas to study these variations, when possible, given the limited number of solutions in some regions. We also created different sets where we only considered the best quality solutions. Unfortunately, the number of best quality solutions was limited in most areas, and therefore it was not possible to run inversion using only those mechanisms. However, by comparing the results between data sets where it was possible to run both inversions, the differences were not significant, suggesting that it is appropriate to use the focal mechanisms with quality D that composed more than 85% of the solutions.

Overall, the stress field in this region presents temporal variations. To define the periods to be used, we used GPS data to determine the caldera's episodes of uplift and subsidence. The Yellowstone Plateau also displays spatial variations. To describe these

variations, we used the minimum principal stress directions that are horizontal or near horizontal in all the cases as expected for an extensional regime dominated by NE-SW Basin and Range extension in this area. The stress field rotates from an orientation near to N-S near Hebgen Lake fault zone to NE-SW near Norris Junction. In addition, all the regions that fall within the 0.64 Ma caldera display orientations ENE-WSW. The rest of the areas display orientations NE-SW, being consistent with previous studies in the area.

7 Reference List

Christiansen, R. L. (1984). Yellowstone magmatic evolution: Its bearing on understanding large-volume explosive volcanism. Explosive Volcanism: Inception, Evolution, and Hazards, 84-95.

Farrell, J., Husen, S., & Smith, R. B. (2009). Earthquake swarm and b-value characterization of the Yellowstone volcano-tectonic system. Journal of Volcanology and Geothermal Research, 188(1-3), 260-276.

Farrell, J., Smith, R. B., Husen, S., & Diehl, T. (2014). Tomography from 26 years of seismicity revealing that the spatial extent of the Yellowstone crustal magma reservoir extends well beyond the Yellowstone caldera. *Geophysical Research Letters*, *41*(9), 3068-3073.

Hardebeck, J. L., & Shearer, P. M. (2002). A new method for determining first-motion focal mechanisms. *Bulletin of the Seismological Society of America*, *92*(6), 2264-2276.

Hardebeck, J. L., & Shearer, P. M. (2003). Using S/P amplitude ratios to constrain the focal mechanisms of small earthquakes. *Bulletin of the Seismological Society of America*, *93*(6), 2434-2444.

Heimann, Sebastian; Kriegerowski, Marius; Isken, Marius; Cesca, Simone; Daout, Simon; Grigoli, Francesco; Juretzek, Carina; Megies, Tobias; Nooshiri, Nima; Steinberg, Andreas; Sudhaus, Henriette; Vasyura-Bathke, Hannes; Willey, Timothy; Dahm, Torsten (2017). Pyrocko - An open-source seismology toolbox and library. V. 0.3. GFZ Data Services. http://doi.org/10.5880/GFZ.2.1.2017.001

Huang, H. H., Lin, F. C., Schmandt, B., Farrell, J., Smith, R. B., & Tsai, V. C. (2015). The Yellowstone magmatic system from the mantle plume to the upper crust. Science, 348(6236), 773-776.

Husen, S., & Smith, R. B. (2004). Probabilistic earthquake relocation in three-dimensional velocity models for the Yellowstone National Park region, Wyoming. *Bulletin of the Seismological Society of America*, *94*(3), 880-896.

Husen, S., Smith, R. B., & Waite, G. P. (2004). Evidence for gas and magmatic sources beneath the Yellowstone volcanic field from seismic tomographic imaging. *Journal of Volcanology and Geothermal Research*, *131*(3-4), 397-410.

Lin, G., & Okubo, P. G. (2016). A large refined catalog of earthquake relocations and focal mechanisms for the Island of Hawai'i and its seismotectonic implications. *Journal of Geophysical Research: Solid Earth*, *121*(7), 5031-5048.

Lomax, A., Virieux, J., Volant, P., & Berge-Thierry, C. (2000). Probabilistic earthquake location in 3D and layered models. In *Advances in seismic event location* (pp. 101-134). Springer, Dordrecht.

Maury, J., Cornet, F. H., & Dorbath, L. (2013). A review of methods for determining stress fields from earthquakes focal mechanisms; Application to the Sierentz 1980 seismic crisis (Upper Rhine graben). *Bulletin de la Societe Geologique de France*, *184*(4-5), 319-334.

Moser, T. J., Van Eck, T., & Nolet, G. (1992). Hypocenter determination in strongly heterogeneous earth models using the shortest path method. *Journal of Geophysical Research: Solid Earth*, *97*(B5), 6563-6572.

Murray, J. R., & Svarc, J. (2017). Global Positioning System data collection, processing, and analysis conducted by the US Geological Survey Earthquake Hazards Program. Seismological Research Letters, 88(3), 916-925.

Perkins, M. E., & Nash, B. P. (2002). Explosive silicic volcanism of the Yellowstone hotspot: The ash fall tuff record. Geological Society of America Bulletin, 114(3), 367-381.

Russo, E., Waite, G. P., & Tibaldi, A. (2017). Evaluation of the evolving stress field of the Yellowstone volcanic plateau, 1988 to 2010, from earthquake first-motion inversions. Tectonophysics, 700, 80-91.

Russo, E., Tibaldi, A., Waite, G. P., Bonali, F. L., Massin, F., & Farrell, J. (2020). Unraveling the complex deformation pattern at Yellowstone plateau through seismicity and fracture analysis. Tectonophysics, 778, 228352.

Shelly, D. R., Hardebeck, J. L., Ellsworth, W. L., & Hill, D. P. (2016). A new strategy for earthquake focal mechanisms using waveform-correlation-derived relative polarities and cluster analysis: Application to the 2014 Long Valley Caldera earthquake swarm. *Journal of Geophysical Research: Solid Earth*, *121*(12), 8622-8641.

Shelly, D. R., & Hardebeck, J. L. (2019). Illuminating faulting complexity of the 2017 Yellowstone Maple Creek earthquake swarm. Geophysical Research Letters, 46(5), 2544-2552.

Shen, Y., Forsyth, D. W., Conder, J., & Dorman, L. M. (1997). Investigation of microearthquake activity following an intraplate teleseismic swarm on the west flank of the southern East Pacific Rise. *Journal of Geophysical Research: Solid Earth*, *102*(B1), 459-475.

Smith, R. B., Jordan, M., Steinberger, B., Puskas, C. M., Farrell, J., Waite, G. P., ... & O'Connell, R. (2009). Geodynamics of the Yellowstone hotspot and mantle plume: Seismic and GPS imaging, kinematics, and mantle flow. Journal of Volcanology and Geothermal Research, 188(1-3), 26-56.

Stein, S., and M. Wysession, (2009). An Introduction to Seismology, Earthquakes, and Earth Structure, Chapter 4: Earthquakes, Wiley-Blackwell Publishing, ISBN: 978-1-4443-1131-0.

Tarantola, A., & Valette, B. (1982). Inverse problems= quest for information. Journal of geophysics, 50(1), 159-170.

Trugman, D. T., & Shearer, P. M. (2017). GrowClust: A hierarchical clustering algorithm for relative earthquake relocation, with application to the Spanish Springs and Sheldon, Nevada, earthquake sequences. *Seismological Research Letters*, *88*(2A), 379-391.

Vavryčuk, V. (2014). Iterative joint inversion for stress and fault orientations from focal mechanisms. *Geophysical Journal International*, *199*(1), 69-77.

Waite, G. P., & Smith, R. B. (2004). Seismotectonics and stress field of the Yellowstone volcanic plateau from earthquake first-motions and other indicators. Journal of Geophysical Research: Solid Earth, 109(B2).

Waite, G. P., Smith, R. B., & Allen, R. M. (2006). VP and VS structure of the Yellowstone hot spot from teleseismic tomography: Evidence for an upper mantle plume. Journal of Geophysical Research: Solid Earth, 111(B4).

White, B. J. P., Smith, R. B., Husen, S., Farrell, J. M., & Wong, I. (2009). Seismicity and earthquake hazard analysis of the Teton–Yellowstone region, Wyoming. Journal of Volcanology and Geothermal Research, 188(1-3), 277-296.

Wittlinger, G., Herquel, G., & Nakache, T. (1993). Earthquake location in strongly heterogeneous media. *Geophysical Journal International*, *115*(3), 759-777.

Yang, W., Hauksson, E., & Shearer, P. M. (2012). Computing a large refined catalog of focal mechanisms for southern California (1981–2010): Temporal stability of the style of faulting. Bulletin of the Seismological Society of America, 102(3), 1179-1194.